Correspondence to:
A. Cislaghi,
alessio.cislaghi@unimi.it

Field Measurements of Passive Earth Forces in Steep, Shallow, Landslide-Prone Areas

Alessio Cislaghi[1] , **Denis Cohen[2]** , **Eric Gasser[3]** , **Gian Battista Bischetti[1,4]** , and **Massimiliano Schwarz[3,5]**

[1]Department of Agricultural and Environmental Sciences (DiSAA), University of Milan, Milan, Italy, [2]Department of Earth and Environmental Science, New Mexico Tech, Socorro, NM, USA, [3]Department of Agronomy, Forestry, and Food Sciences, Bern University of Applied Sciences, Zollikofen, Switzerland, [4]Centre of Applied Studies for the Sustainable Management and Protection of Mountain Areas (Ge.S.Di.Mont), University of Milan, Edolo, Italy, [5]ecorisQ, International Association for Natural Hazard Risk Management

Abstract Passive earth resistance plays an important role in slope stability analyses for predicting shallow landslide susceptibility. Three-dimensional models estimate the contribution of this factor to slope stability using geotechnical theories designed for retaining structures and add it to the resistive forces. Systematic investigations have not been conducted to quantify this resistance in soils experiencing compression during the triggering of shallow landslides. This study presents field-scale experimental data of passive earth force for cohesive and frictional clayey gravel evaluated at different combinations of soil depths and slopes. The experimental setup included a specialized device composed of a steel structure and a stiff plate that moved toward a mass of soil. In both dynamic and quasi-static states, force-displacement curves and maximum compression resistance were determined for several water content conditions induced by a rainfall simulator. The maximum dynamic force ranged from 8.49 to 31.67 kN for soil depths ranging between 0.36 and 0.50 m, whereas the quasi-static force corresponded to 60% of the dynamic force. Furthermore, rainfall generated an additional decrease of compression resistance compared to that measured in the field. A comparison of measured data with theoretical models of passive earth force indicated that Rankine's solution provided the best estimate, whereas the logarithmic spiral approach significantly overestimated passive earth force by up to 70%. Therefore, the correct choice of geotechnical formulation or the direct use of field measurements to estimate passive earth force may significantly improve the accuracy of 3-D limit equilibrium models for assessing slope stability over natural landscapes.

1. Introduction

Shallow landslides are a significant hazard in mountain areas due to their high frequencies and forecasting difficulties (Campbell, 1975; Kim et al., 2015; Mao et al., 2012). These phenomena control landscape evolution as major landform-shaping processes (Korup, 2006; Korup et al., 2010; Larsen et al., 2010; Roering et al., 2001, 2005; Shroder & Bishop, 1998) and are often associated with numerous natural events, such as soil instabilities (e.g., debris flow and soil slip) and various channel processes (e.g., transport of large woody debris and sediment during floods) (Sidle & Ochiai, 2006). Predicting the location of shallow landslides at the regional scale is a fundamental challenge for the scientific community, and numerous models have been developed, ranging from statistically based approaches to physically based spatially distributed models (Brenning, 2005; Cislaghi et al., 2017; Guzzetti et al., 1999; Mergili et al., 2014; Montgomery & Dietrich, 1994; Pradhan, 2010). The latter provides a better understanding of the triggering processes and thus is more suitable for designing appropriate measures to mitigate the consequences of instability phenomena (van Beek & van Asch, 2004). Most of these approaches are based on the 1-D infinite slope stability model (Taylor, 1948) and a simple steady state assumption for hydrological soil conditions (Montgomery & Dietrich, 1994; Pack et al., 1998; Wu & Sidle, 1995). Some of these models include the stabilizing role provided by root systems that cross the sliding surface and integrate this factor as an additional apparent soil cohesion element called basal root reinforcement (Burroughs & Thomas, 1977; Sidle et al., 1985). The 1-D approach has been largely used in practice, and recent studies have verified that the results provided by the infinite slope analysis converge to those of finite element models only when the landslide length-to-thickness ratio largely exceeds 16

(>16: Griffiths et al., 2011; >25: Milledge et al., 2012). Moreover, Montgomery et al. (2009) found incompatibility between monitored field observations and model predictions using measured site properties in the infinite slope model and highlighted the need to include friction and root reinforcement acting on the lateral sides of the potential landslide (i.e., the so-called lateral root reinforcement). Recently, Prancevic et al. (2018) reproduced the initialization of 90 landslides in an experimental flume using cohesionless soils and observed how the boundary stress, particularly the stress associated with short landslides, caused increases in water levels, which were needed to trigger the mass movement and limited the involved soil thickness. In summary, some criticisms and limits of applicability related to the 1-D methods remain mainly because of the absence of boundary interactions (e.g., Casadei et al., 2003; Montgomery et al., 2000; Reneau & Dietrich, 1987; Schmidt et al., 2001).

In the 1980s, to overcome such significant limitations, Riestenberg and Sovonick-Dunford (1983) developed a more appropriate model for shallow landslides on vegetated slopes that incorporated soil cohesion and root strength acting on the basal area and lateral area of the element involved with failure at the scarp; however, this model neglected lateral frictional resistance and soil suction along element margins. Afterward, Burroughs (1985) developed a pioneering 3-D geotechnical model and proposed a simplified limit equilibrium force balance on a slope block undergoing translational motion assuming that failure occurs simultaneously with shearing at the boundaries without internal deformation. This model evaluates the factor of safety of each block, including rooted soil cohesion on all sides, earth pressures on lateral sides, active earth pressure on the upslope side, and passive earth pressure on the downslope side. Earth pressures are calculated using the Mohr diagram (Taylor, 1948).

Based on such concepts, many studies have proposed a 3-D slope stability model in a raster-based GIS environment to predict the location and size of shallow landslides by taking vegetation effects into account (Dietrich et al., 2007; Terwilliger & Waldron, 1991). Furthermore, these models were combined with complementary algorithms, such as a spectral clustering search algorithm (Milledge et al., 2014; Bellugi, Milledge, Dietrich, McKean, et al., 2015; Bellugi, Milledge, Dietrich, Perron, et al., 2015), a process-based fully distributed hydrological model (Anagnostopoulos et al., 2015), a stochastic procedure (Cislaghi et al., 2017, 2018; Cislaghi & Bischetti, 2019; Dorren & Schwarz, 2016), and a seismicity component (Hess et al., 2017). Recently, Cohen and Schwarz (2017) implemented the software SOSlope, which is based on force-displacement calculations of rooted soils under tensile and compressive states using the discrete element method.

An alternative approach for treating the downslope boundary was included in a hydromechanical model proposed by Lehmann and Or (2012), and it has been adopted in subsequent studies (Fan et al., 2016; von Ruette et al., 2013) and was based on the concept of *landslide fluidization* (e.g., Ochiai et al., 2004). This failure mechanism occurs when a soil mass in a near-saturation condition and under a compressive load exceeds the ultimate compressional resistance and causes destruction of the soil matrix, thereby increasing the pore water pressure and reducing the effective stress. Their proposed approach consisted of a basic formal condition for soil fluidization defined by a water-dependent compressive strength (Mullins & Panayiotopoulos, 1984). However, Milledge et al. (2014) suggested that although this approach may be appropriate for unconfined slopes, it may be less appropriate for natural landscapes because it completely ignores those forces on the margins due to the weight of soil. In addition, it is unclear when this type of behavior occurs in nature. Furthermore, recent studies have shown the effects of passive earth forces on landslide triggering (e.g., Cohen & Schwarz, 2017).

To include such earth pressures, 3-D models have generally adopted conventional geotechnical calculations commonly used for the design of engineering structures, such as retaining walls, sheet-pile walls, and braced and unbraced excavations (Bowles, 1997). Although such approaches date back to the eighteenth and nineteenth centuries (e.g., Coulomb, 1776; Culmann, 1886; Rankine, 1857; Rebhann, 1871), only a few studies have compared analytical calculations of earth pressures with field observations or laboratory experiments. Terzaghi (1920) measured the horizontal and vertical components of the passive earth force using a box of dry sands and a 0.05-m-high wall on one side. Later, Fang et al. (1994, 1997, 2002) conducted experiments with a similar experimental setup but different cohesionless soils and several backfill inclinations. Recently, Schwarz et al. (2015) investigated the effect of roots on compression resistance by compressing rooted and nonrooted soils using a custom-designed experimental laboratory setup. Notwithstanding
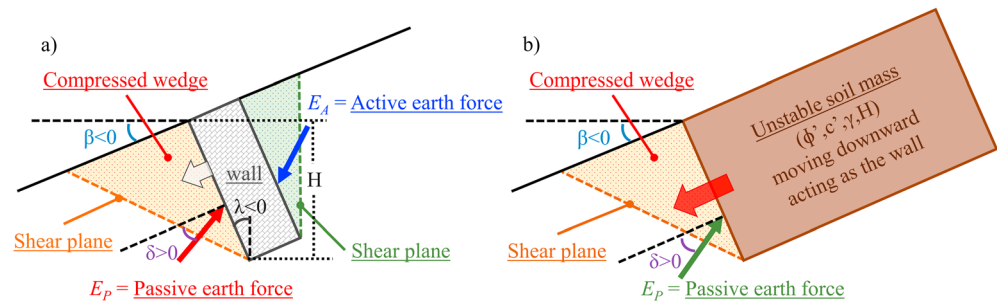
Figure 1. Schematic representation of the passive earth wedge (modified from Schwarz et al., 2015): (a) in the classical geotechnical literature and (b) in landslide modeling. Symbols are defined in the Notation section.

these studies, data regarding soil behavior under compression are scarce and usually limited to cohesionless soils under artificial conditions (i.e., in the laboratory). In this context, our study objectives are as follows:

1. Investigate the passive earth force-displacement relationship in field experiments with cohesive soil under loading;
2. Analyze the rheology and the state of stress at the toe of a creeping landslide (where alternating periods of motion and quasi-static conditions occur before failure) by recording differences between passive earth forces in motion versus those under quasi-static conditions by interrupting the compression thrust at different time steps;
3. Compare the maximum measured passive earth resistance with theoretical calculations commonly used in geotechnical practice;
4. Verify the external factors (e.g., soil depth, hillslope inclination, and soil water content) that influence the resistive force;
5. Measure the geometrical characteristics, particularly the change of surface topography and the volume of soil involved in the compressed wedge, during the progression of the experiment to determine the boundary effects.

These innovative measurements illustrate the physical process of compression force mobilization, which can occur during landslide failure. Finally, this study may be an important step for improving 3-D slope stability approaches and broadening the analysis to larger scales (i.e., hillslope, watershed, and regional scales).

2. Literature Review of Passive Earth Force

The 3-D limit equilibrium models included the calculation of the boundary earth forces through conventional formulations typically used in the design of retaining structures in the field of soil mechanics. Several methods are available in the geotechnical literature to estimate passive earth forces, such as limit equilibrium solutions (Janbu, 1957; Krey & Ehrenberg, 1936; Patki et al., 2015), plasticity theory (Chen & Rosenfarb, 1973), empirical equations (e.g., Brinch Hansen, 1953), the finite element model (Duncan & Mokwa, 2001), and the finite difference computer method (Benmebarek et al., 2008). The first pioneering studies developed by Coulomb (1776) and Rankine (1857) were performed beginning at the end of the eighteenth century and were based on similar assumptions: (1) soil is isotropic, homogeneous, and cohesionless; (2) rupture surfaces are a plane; (3) compressed wedges have a planar surface (i.e., the backfill inclination angle β is zero; see Figure 1 for a schematic of the compressed wedge); (4) friction resistance is distributed uniformly along the rupture plane; (5) failure of the wedge is a rigid body undergoing translation; and (6) failure is a plane strain problem.

Following all these assumptions, Coulomb's and Rankine's theories provided a closed-form solution for evaluating the coefficient of passive earth pressure K_P as follows:

$$K_P = \tan^2\left(\frac{\pi}{4} + \frac{\phi'}{2}\right)$$

(1)

where ϕ' is the soil internal friction angle.

These approaches are commonly used in geotechnical practice and were included in the pioneering 3-D slope stability models (e.g., Dietrich et al., 2007). However, many authors have observed and

demonstrated that certain assumptions are too constraining, such as a vertical retaining wall and a horizontal backfill (Benmeddour et al., 2012; Craig, 2013; Das, 2010; Fang et al., 1997; Kérisel & Absi, 1990; Terzaghi, 1943), and they have proposed modifications and improvements to include other configurations. For example, Müller-Breslau (1906) generalized Coulomb's theory for cohesionless soils, and it also considers a backfill inclination (β), the frictional interaction angle between the wall and soil (δ), and the angle of the internal face between the wall and vertical direction (λ). This solution was implemented within the model proposed by Terwilliger and Waldron (1991). As an alternative, based on the Rankine stress state in a semi-infinite mass of cohesive soil with inclined backfill, Mazindrani and Ganjali (1997) proposed an analytical closed-form solution for evaluating K_P (equation (2); called gen-Rankine in the present study) and included it in a simpler formulation for calculating E_P (equation (3)).

$$K_P = \frac{1}{\cos^2(\phi')}\left\{ \frac{2\ \cos^2(\beta) + 2\left(\frac{c}{\gamma H}\right)\cos(\phi')\sin(\phi') +}{\sqrt{\begin{array}{c} 4\ \cos^2(\beta)\left[\cos^2(\beta) - \cos^2(\phi')\right] + 4\left(\frac{c}{\gamma H}\right)^2\cos^2(\phi') + \\ 8\left(\frac{c}{\gamma H}\right)\cos^2(\beta)\cos(\phi')\sin(\phi') \end{array}}} \right\} - 1 \tag{2}$$

$$E_P = \frac{1}{2}\gamma H^2 K_P \tag{3}$$

where γ is the unit of soil weight, H is the soil depth, and c is the soil cohesion.

Alternately, substantial errors are associated with the assumption of a triangular distribution of earth pressure on the retaining wall and the planner failure surface on which Coulomb's and Rankine's theories are based. Indeed, many authors have shown that the distribution of earth pressure depends on the wall movement and friction interaction angle between the soil and wall, which generates a nonlinear distribution along the wall (e.g., Fang et al., 1994). Moreover, they approximated the real failure surface as a combination of a curve and a straight line (Chen & Rosenfarb, 1973; Krey & Ehrenberg, 1936; Terzaghi, 1941), an elliptical line (Caquot & Kérisel, 1948), or a logarithmic spiral and a straight line (Janbu, 1957). Soubra et al. (1999) developed a variational limit equilibrium method that combines a moment equilibrium equation with a logarithmic spiral failure surface. This wedge geometry provides a more accurate prediction than the planar failure surface models (Kumar & Subba Rao, 1997). Soubra and Macuh (2002) developed a spreadsheet tool for general cases (i.e., sloping backfill, frictional and cohesive soil, and uniform surcharge) called the log-spiral approach, which is described in more detail in Appendix A. The log-spiral approach was first integrated into a 3-D slope stability model developed by Milledge et al. (2014), and it proposed the coefficients $K_{P\gamma}$, K_{Pq}, and K_{Pc} to represent the effects of soil weight, vertical surcharge loading, and cohesion, respectively. The passive earth force can be expressed as follows:

$$E_P = K_{P\gamma}\frac{\gamma H^2}{2} + K_{Pq}qH + K_{Pc}cH \tag{4}$$

where q is the vertical surcharge loading.

Most studies on the calculation of passive earth force neglect the effects of the third dimension. Blum (1932) conducted the first study focused on this issue. Blum's formulation is an extension of the traditional one-block Coulomb mechanism that uses the limit equilibrium solution, which neglects the frictional forces acting on lateral planes. Later, Soubra et al. (2000) and Soubra and Regenass (2000) analytically investigated several translation failure wedges (pentahedral single rigid block and multiblock mechanisms) using the limit equilibrium analysis to evaluate K_P. Their results emphasized that a multiblock mechanism composed by pentahedrons and truncated by two portions of right circular cones best represented the failure volume and generated accurate and reliable solutions for practical use when compared to Blum's approach. Meanwhile, Regenass et al. (2000) reviewed the numerical and experimental studies of the 3-D solution and proposed a synthesis based on the previous study of Horn (1972), and they highlighted the wide

variability in quantifying the effect of the third dimension, which is mainly due to different tested soils, different experimental setups, and the lack of a standard procedure. Nevertheless, they presented a simple empirical formulation:

$$K_{P-3D} = K_P \left(1 + C \frac{H}{B} \right) \tag{5}$$

where K_{P-3D} is the 3-D coefficient of passive earth pressure, B is the wall width and C is a shape factor (dimensionless) that varies in the literature from 0.04 to 1.37 and presents an average value of 0.52 for H/B less than 1 (Regenass et al., 2000).

Later, Škrabl and Macuh (2005) presented an approach based on 3-D, kinematically admissible, rotational, and hyperbolical failure mechanisms composed of one central and two lateral bodies and evaluated it using the framework of the limit analysis theory. Škrabl (2008) improved the previous version by implementing a 3-D logarithmic spiral. Another similar approach was proposed by Vrecl-Kojc and Škrabl (2007), who applied the upper bound theorem of limit analysis considering a kinematically admissible failure geometry subdivided into three simplified rigid blocks. The main difference of this approach compared to other models is that the lateral parts are composed of a family of cone envelopes. Other studies used the explicit finite difference code FLAC^{3D} (Fast Lagrangian Analyses of Continua in 3 Dimensions) to investigate the 3-D passive earth pressures induced by the translation of a rigid rough retaining wall for associative soils and an increase in the passive earth coefficient with decreasing wall width (Benmebarek et al., 2008; Khelifa & Benmebarek, 2014). More recently, Motta and Raciti (2014) estimated 3-D effects through a practical closed-form solution only applicable for cohesionless soil.

3. Materials and Methods

3.1. Study Area

The selected study site for the field measurements is located in a forested area (WGS84, latitude 46.8160N, longitude 7.8235E) on the north facing slope of the Honegg ridge near the village of Schangnau in the Emmental (Canton of Bern, Swiss Prealps, Switzerland). The average elevation is approximately 1,000 m above sea level, and the mean slope is approximately 25°. The climate is humid continental, which is typical of Central Alpine north facing slopes, the annual precipitation ranges from 1,500 and 1,700 mm, and the mean annual air temperature is approximately 6.5 °C.

The study site is located at the southern boundary of the Molasse basin at the border of the Subalpine Molasse (clastic sedimentary rocks). The soil thickness is approximately 2 m on average, and rock fragments are generally present at soil depths between 0.30 and 0.50 m. The deeper soil layer mainly consists of Pleistocene moraine material that was deposited during the last glacial maximum by the Emme glacier, and the shallower soil layer above it is composed of a Holocene weathered hillside regolith (geological map of Switzerland 1:25000, Swiss Federal Office of Topography, www.swisstopo.admin.ch, 2012). Moreover, mudflow material was likely periodically deposited on the surface of the study area and mobilized by severe shallow landslides and debris flows. Such instabilities generally involved a soil surface layer up to 0.60 m in depth and an inclination varying from 20° to 40°.

The study area is almost completely covered by a coniferous forest, where European spruce (*Picea abies* (L.) Karst) and silver fir (*Abies alba* Mill.) are the predominant species (70% and 30%, respectively); however, European beech (*Fagus sylvatica* L.) and sycamore maple (*Acer pseudoplatanus* L. [1753]) are also present. A nearly homogeneous forest canopy covers approximately 80% of the ground, and it is seldom interrupted by small gaps. This forest is managed as a protection forest for slope stabilization and for soil protection from erosion in agreement with the Swiss national directives (Frehner et al., 2005).

3.2. Soil Properties

The soil properties of the study site were determined by analyzing one cubic meter of soil excavated from the A horizon within the top 0.40 m as described in detail by Schwarz et al. (2015). The grain size distribution, Atterberg's consistency limits, and Proctor compaction test were carried out in the laboratory to measure the density and water content of the soil subsamples (Table 1). According to the Unified Soil Classification System, the soil was classified as a clayey gravel with sand. Additionally, the coefficient of uniformity C_{Ud}

Table 1
Mechanical Properties of the Soil at the Experimental Site

Symbol	Mechanical property	Unit of measure	Values
c_C	Content of clay	% by mass	6.2
c_M	Content of silt	% by mass	34.6
C	Content of sand	% by mass	28.6
c_G	Content of gravel	% by mass	30.7
C_{ud}	Coefficient of uniformity	—	87.3
C_{Cd}	Coefficient of curvature	—	0.9
W_L	Water content at liquid limit	% by mass	33.2
W_P	Water content at plastic limit	% by mass	22.5
I_P	Plastic index	% by mass	15.3
W_{Pr}	Optimum water content	% by mass	15.3
ρ_{Pr}	Material's maximum density	g/cm^3	1.81
D_{Pr}	Material's degree of compaction	%	86.7

Note. The parameters WPr, ρPr, and DPr are derived from a Proctor test on the material's fraction with a particle size of less than 4.0 mm; and WL, WP, and IP are derived from testing the material fraction <0.5 mm. All other parameters are derived from testing the fraction <0.5 mm (modified from Schwarz et al., 2015).

indicated that the first layer of soil was well graded and compressible, and the plasticity index P_I revealed that the consistency was sensitive to the variation of water content. In addition, direct shear tests were conducted to estimate several geotechnical parameters and their variability as a function of soil water content (sc-1, sc-2, and sc-3 in Table 2). Such properties are the bulk density prior to the experiment ρ_B; porosity n; the water content θ with indices g and v, which indicate the gravimetric and volumetric values, respectively; the degree of saturation S_R; the effective angle of internal friction ϕ'; and the effective cohesion c'.

3.3. Field Measurements
3.3.1. Experimental Equipment

The compression experiments were carried out using an experimental setup as described in Schwarz et al. (2015) and specifically adjusted for field tests (Figure 2). The compression machine is composed of a steel structure, a stiff plate, and an electromechanical actuator. The dimensions of the steel structure are $1.10 \times 0.72 \times 0.60$ m. The stiff plate is 0.02-m thick, 0.72-m wide, and 0.38-m high, and it is attached to an in-feed slide. Inside the steel structure, an electromechanical actuator (MecVel, AV3 model) moves the stiff plate in a horizontal direction through two sets of two roller bearings sliding on four tracks at a constant velocity of 5 mm/s to a maximum stroke of 0.40 m. The electromechanical actuator requires a power supply of 400 V produced by a gasoline-electric power generator (Kraftech, KT-8500W-Mobile). The compression machine is equipped with (i) a displacement sensor (Burster GmbH, potentiometric displacement sensor model 8719, accuracy ±0.05%) to measure the displacement parallel to the machine inclination (i.e., parallel to the hillslope inclination), (ii) four load cells (Burster GmbH, miniature ring load cell model 8438, 50 kN, accuracy <1%) located on the four edges of the stiff plate, and (iii) a data logger (Campbell Scientific, CR1000) to record and store the measurements at time intervals of 1 s. The displacement sensor was calibrated using five fixed points, whereas load cells were calibrated with known weights. In addition, five soil moisture sensors (Decagon, 10HS, ±3% accuracy by volume) were positioned at a depth of 0.10 m, with three at 0.15 m and two at 0.30 m from the stiff plate to monitor the volumetric water content. The measurements were recorded every 60 s using another data logger (Decagon, Em50).

During each experiment, three scans of the ground surface were performed using a laser scanner (FARO, Focus 3-D model). The scanner completes a scan in 25 min with a scan speed of 244,000 dots per second and a resolution of 1.50 million dots per square meter. The accuracy is ±2 mm for a distance between the scanner and object ranging from 10 to 25 m.

To determine the effects of rainfall on the passive earth force, the superficial ground was irrigated during a number of compression experiments using a rain simulator, which consisted of a square aluminum plate (1.00×1.00 m) with small tubes attached to 100 perforated holes. The tubes were mounted in a 0.10×0.10 m square pattern and had inner diameters of 2 mm that led to a small cylindrical reservoir.

Table 2
Soil Shear Parameters for Three Samples With Different Water Contents (sc-1, sc-2, and sc-3)

Sample	ρ_B (g/cm^3)	n (m/m^3)	θ_g (% by mass)	θ_v (m/m^3)	S_R (m/m^3)	ϕ' (deg)	c' (kN/m^2)
sc-1	1.57	0.420	19.43	0.304	0.725	23.7	21.6
sc-2	1.56	0.421	22.84	0.357	0.849	24.1	18.1
sc-3	1.561.56	0.424	27.22	0.423	0.998	27.1	13.5

Note. Three samples of the fraction <0.5 mm were tested at a shearing rate of 0.04 mm/s; ρ_B is the bulk density measured prior to the experiment when the soil was formed in the device; n is porosity; ϑ is the water content with indices g and v, which indicate gravimetric and volumetric values, respectively; S_R is the degree of saturation; ϕ' is the effective angle of internal friction; and c' is the effective cohesion (modified from Schwarz et al., 2015).
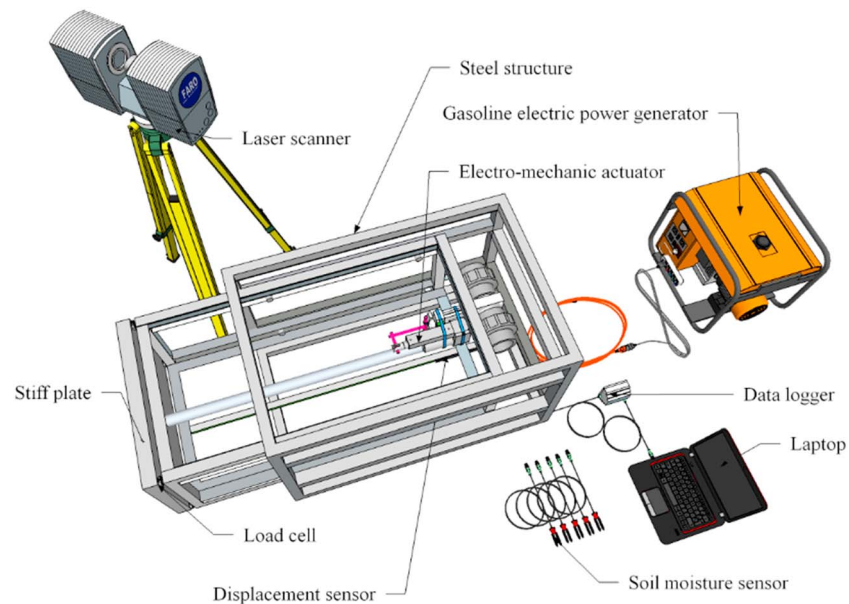
Figure 2. Schematic drawing of experimental equipment that consists of a steel structure, a stiff plate, and an electromechanical actuator powered by a gasoline-electric power generator and equipped with a displacement sensor, four load cells, five soil moisture sensors, a data logger, and a laser scanner.

During the irrigation, an electric motor moved the plate back and forth by 0.05 m and a flow meter controlled the intensity of the rainfall. The rain simulator was fed by a water-filled tank through a hydraulic pump. According to Lange et al. (2009, 2011), the recommended distance between the plate and soil surface lies between 0.30 and 0.50 m.

3.3.2. Experimental Design and Procedure

Eleven sites with topographical characteristics (i.e., aspect and inclination) similar to those areas hit by shallow landslides were selected on the same hillside and at a known distance from tree trunks to minimize the presence of roots for easy digging and reduce the effects of roots on the compression force (see section 3.3.3.2). The experiments aim to measure the soil compression force F_P as a function of H, β, θ_v, and displacement Δx. The experimental procedure consisted of several field operations as shown in Figure 3 via photographs. First, the upper 0.10 m of the superficial soil layer, which was mainly composed of organic matter, was removed. Then, a trench with a size of 1.20×1.00 m and depth of approximately 0.50 m was manually excavated with shovels and pickaxes, and care was taken to prevent damage to the root system. Once the trench was excavated, roots crossing the downslope profile were counted and their diameters were measured using an electronic caliper. Additionally, the compression machine was assembled with all sensors and the data logger and placed in the trench. Then, the compression machine was fixed on the upslope side using a wooden plate and two wooden sticks, and backfill was added and compacted with soil and stones. This anchorage served to prevent uphill movement of the machine and facilitate measurements of only the displacement in the same direction as the mechanical thrust. Throughout the experiment, the inclination of the compression machine was monitored using an accelerometer. Five soil water content sensors were introduced into the soil. Before each experiment (*control*), the laser scanner scanned the soil surface in front of the compression machine to create a 3-D image.

The compression experiment consisted of a series of *loading steps* during which the soil was displaced by 0.05 m. After every 0.05 m of displacement, the loading step was interrupted by a *pause*. The experiment started through the activation of the electromechanical actuator that moved the compression plate toward the downhill soil with a constant velocity of 5 mm/s. The selected velocity was a compromise between the characteristics of the electromechanical actuator, data acquisition, and experimental duration. The pauses allowed for the measurement of the compression force for three conditions: (1) when failure deformations occurred under reciprocated dynamic force; (2) a lack of deformation or displacement; and (3) all forces

Figure 3. (a) Flowchart of the experimental procedure and (b) photographs at different stages of the experiment.

simultaneously tending toward equilibrium. The first condition represents the effects of *dynamic* force. Conversely, the second condition is comparable to the rigorous static state, which is a key assumption in the geotechnical theories. In the present manuscript, this last condition was named a *quasi-static* state. In addition, considering the scientific knowledge about the rheological properties of soils (Ghezzehei & Or, 2001, 2003), a linear relationship between the soil shear strength and displacement rate may be assumed (i.e., velocity). Thus, the tested range of velocities between 0 (quasi-static state) and 5 mm/s (dynamic condition) covers a plausible range of values that were expected during the triggering of shallow landslides, which allows for the calibration of a rheological model for the soil under the tested conditions. The loading step was repeated after a minimum pause of 25 min up to a maximum displacement of 0.35 m. During the pauses, three scans were conducted: at the beginning (control), at the second pause (*pause-2*), and at the end of each experiment. The duration of each pause was set based on laboratory tests conducted by Schwarz et al. (2015), as well as results of initial experiments at the side and the time required to complete a scan of the surface.

The experiments simulated the progression of the compressive state of stress at the toe of an active landslide (i.e., the downslope boundary condition). Indeed, prior to failure, an upward sliding soil mass progressively generated an increase of compression loading at the downslope boundary. When such a compressive state of strength exceeds the maximum passive earth resistance, the soil mass starts again to move downslope until it reaches a stabilized state. This process is especially evident in the case of creeping or constrained landslides (Doglioni et al., 2011; Friedli et al., 2017; Oberender & Puzrin, 2016; Puzrin & Schmid, 2011).

For the experiments with simulated rainfall, the irrigation started after pause-2. The rainfall simulator was positioned above the downslope wedge in front of the compression machine. Each irrigation event lasted for approximately 60 min, and the volume flux density of irrigation was 70 mm/hr. This amount of rainfall corresponds to the maximum hourly precipitation rate with a return period of 100 years for this region (Lange et al., 2009).

3.3.3. Data Processing

3.3.3.1. Effects of Interface Friction

The mobilization of compression resistance occurs when a soil wedge moves downward along a hillslope. This process depends on several factors, such as (i) the amount and direction of movement, (ii) strength and stiffness of soil, and (iii) friction/adhesion between the pushing soil wedge and the compressed one (Duncan & Mokwa, 2001). The experimental design of this study allows for the measurement of the component of the compression force perpendicular to the stiff plate $F_{P\perp}$ with four load cells located at its corners. However, the interfacial friction between the plate and the soil modifies the direction of the compression machine (Bowles, 1997). To correct this effect, it is necessary to estimate the angle δ.

$$F_P = \frac{F_{P\perp}}{\cos(\delta)} \tag{6}$$

The angle δ is known as the interface friction angle and indicates the orientation of F_P with respect to the perpendicular direction with respect to the movement of the stiff plate (equation (7)).

$$\delta = \text{atan}\left(\frac{F_{P_{\parallel}}}{F_{P\perp}}\right) \tag{7}$$

where $F_{P_{\parallel}}$ is a component of F_P that acting parallel to the compression plate and $F_{P\perp}$ is the component acting perpendicular to the compression plate that was measured by the load cells.

Assuming a quasi-static equilibrium among all forces acting on the compression machine, that is, at the end of each pause, it is possible to evaluate the equilibrium among the parallel component of all acting forces with respect to the direction of plate movement as follows:

$$\delta = \text{atan}\left(\frac{W_{\text{CM}}\cos\alpha - \sum R}{F_{P\perp}}\right) \tag{8}$$

where W_{CM} is the weight of the compression machine, α is the inclination of the compression machine, and ΣR is the sum of the reaction forces. However, except for the reaction force under the weight of the compression machine, the other reaction forces could not be measured. Consequently, equation (8) became an upper bound solution for estimating the magnitude of δ. For more details, see Text S1 in the supporting information.

3.3.3.2. Effects of Roots

In this study, the measurements of passive earth force in rooted soils include the contribution of roots under compression. Such additional root reinforcement is mobilized across the shear plane developed during compression, and it leads to a complex bending-buckling-tensioning of the roots (Wu et al., 1988). To evaluate this effect, Schwarz et al. (2015) proposed an adapted fiber bundle model for roots under compression called Co-RBMw (Compressed-Root Bundle Model Weibull). They assumed that the maximum root-buckling force can be estimated as a function of the root diameter (ϕ) using a two-parameter power law function:

$$F_{rb}^{ult} = F_0\phi^{\xi} \tag{9}$$

where F_{rb}^{ult} is the maximum buckling-tensile force, ξ is the empirical exponent, and F_0 is a multiplicative constant. This model considers the root reinforcement as a function of displacement, root diameter distribution, and a cumulative Weibull probability distribution of root strength within a single root diameter class. Consequently, it estimates the total contribution of a root bundle to the compression force F_{rb-tot} by

summing up the force provided by each root diameter class i, that is, $F_{rb-i}(\phi_i, \Delta x)$, multiplied by the survival function S as follows:

$$F_{rb-\text{tot}}(\Delta x) = \sum_{i=1}^{n_c} N_i F_{rb-i}(\phi_i, \Delta x) S(\Delta x_i^*) \tag{10}$$

where n_c is the number of root diameter class, N_i is the number of roots in class diameter i, ϕ_i is the diameter of root class i, Δx is the displacement, and Δx^* is the displacement normalized by that measured at maximum compression force. $F_{rb-i}(\phi_i, \Delta x)$ is the individual root force that can be estimated using Hooke's law for elasticity:

$$F_{rb-i}(\phi_i, \Delta x) = k(\phi)\Delta x \quad F_{rb-i}(\phi_i, \Delta x) < F_{rb}^{ult}(\phi) \tag{11}$$

where k is the spring constant (dimensionless), which is a function of ϕ through the following linear relationship:

$$k(\phi) = k_i + k_P\phi \tag{12}$$

where k_i and k_p are the two linear parameters (Schwarz et al., 2011).

The constant k incorporates the mechanical properties of the root-soil system under specific conditions (root diameter, tree species, forest stand characteristic, soil properties, soil confining pressure, soil density, and moisture conditions).

The survival function S describes the probability that roots break with increasing displacement and assumes a Weibull probability distribution (Schwarz et al., 2013, 2015):

$$S(\Delta x_i^*) = \exp\left\{-\left[\frac{\Delta x_i k(\phi)}{\sigma F_{rb}^{ult}(\phi)}\right]^\omega\right\} \tag{13}$$

where σ and ω are the scale and shape of the dimensionless Weibull parameters, respectively.

The Co-RBMw model includes six different parameters (F_0, ξ, k_i, k_p, σ, and ω) that have to be calibrated. In this study, the values calibrated by Schwarz et al. (2011, 2013, 2015) were used on the same rooted soil covered system (i.e., the same soil and biomechanical properties). The parameters were $F_0 = 6.5 \times 10^5$ N, $\xi = 1.67$, $k_i = 480$ N/mm, $k_p = 10.2 \times 10^5$ N/mm^2, $\sigma = 1$, and $\omega = 1$. The location of the soil profiles for the compression tests was chosen to minimize the influence of root reinforcement as far away as possible from the tree stems.

3.3.3.3. Dynamic Versus Quasi-Static Force Analysis

The present study investigated the differences between the dynamic and quasi-static force after postprocessing of the measured observations. In fact, the corrected force that corresponds to the dynamic compression force F_{dyn} (equation (14)) was obtained, excluding the effect of interface friction (equation (6)), as well as the contribution of roots to soil resistance (equation (10)).

$$F_{\text{dyn}} = F_P - F_{rb-\text{tot}} \tag{14}$$

The alternation between loading steps and pauses generates a transition state from a dynamic to quasi-static condition. As expected, F_{dyn} instantaneously increases, while the compression machine pushes the stiff plate. In this short period, the rheological characteristics of the soil considerably vary, especially in proximity of the plate (e.g., the porosity decreases while the soil water content and pore pressure increase). During the pause, F_{dyn} asymptotically decreases, dissipating excess pore water pressure, while the compression machine maintains its position. The asymptotic decline is particularly evident when F_{dyn} is normalized by its maximum value and can be described by a three-parameter negative exponential function as follows:

$$F_{\text{dyn}}^* = \frac{F_{\text{dyn}}(t)}{F_{\text{dyn}}^{\max}} = \Lambda t^\Pi + \Gamma \tag{15}$$

where $F_{\text{dyn}}^{\max}$ is the value of F_{dyn} at the interruption of the loading, t is the time, and Λ, Π, and Γ are the three coefficients of the exponential function. The intercept Γ is the asymptotic value corresponding to the ratio between the quasi-static compression force, which is called F_{q-s} hereafter, and $F_{\text{dyn}}^{\max}$.
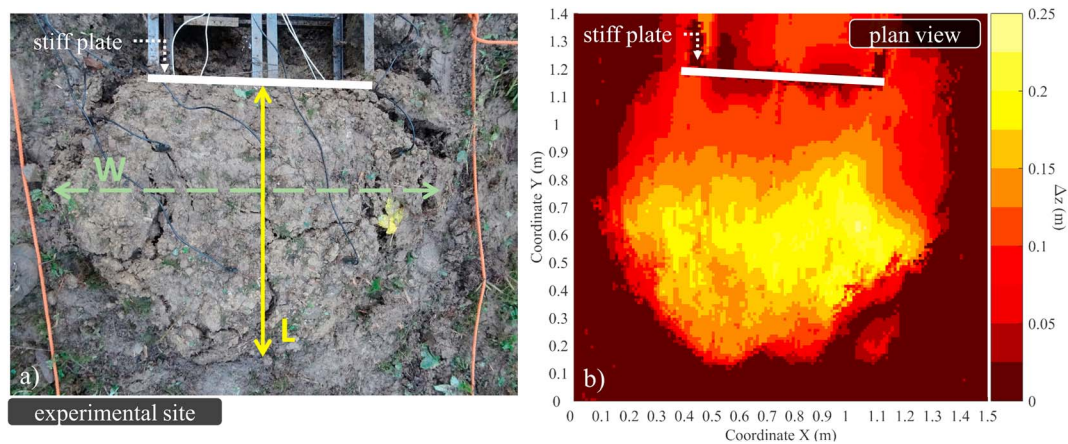
Figure 4. (a) Plan view of one of the experimental sites at the end of the experiment with a maximum displacement of approximately 0.35 m. The compressed wedge and cracks/fractures on the soil surface are clearly visible. (b) Postprocessed image of the soil surface scan. The color scale shows the extension of the compressed wedge and the change in soil surface height. Symbols are defined in the Notation section.

$$\Gamma = \frac{F_{q-s}}{F_{dyn}^{max}} \qquad (16)$$

To compare measurements with theoretical calculations obtained by equations (2)–(4), the maximum values of F_{q-s} were normalized by the length of the stiff plate to obtain the compression force per unit length.

3.3.3.4. Geometry of a Compressed Wedge

Three scans were performed at control, at pause-2 and at the end of each experiment, which corresponded to the initial condition, the maximum compression stage, and the residual compression stage when the sliding soil mass moves downslope, respectively. The scanner-created point clouds were postprocessed using the software PointCab (Point Cloud Software Company GmbH, 2015). The output was a 3-D image and raster map with a resolution of 0.01 m. By differencing the raster maps, changes in the soil surface during the progression of the experiment were measured as well as the extension of the compressed wedge in terms of size and volume. The geometrical measurements consisted of 1-D geometrical characteristics, such as the length L, width W, and difference between the soil surface before and after the experiment Δz. Figure 4 shows a plan-view photograph of one of the experiments and the postprocessed raster, where the color scale emphasizes the extension of the compressed wedge and the values of Δz. In terms of volume, a simple balance allows for evaluation of the 3-D volumetric difference ΔV_{3D} as follows:

$$\Delta V_{3D} = \left(V^* - V_M\right) + \left(V_S - V^*\right) = V_S - V_M \qquad (17)$$

where V^* is the soil volume subject to passive earth pressure, V_M is the moved volume after the movement of the stiff plate, and V_S is the volume difference between control and the next scan. Figure 5 shows a lateral view of the soil mass involved in the experiment in which V^* is the area bordered by the green line, V_M is the yellow area, and V_S is the blue area.

4. Results

4.1. Experimental Measurements

Eleven compression experiments were performed in September–October of 2016, including four under natural conditions (i.e., θ_v is almost constant) and seven tests with simulated rainfall.

H ranged between 0.38 and 0.50 m, and β varied from 13.4° to 28.1°. The soil moisture conditions were determined by measuring θ_v, which ranged between 0.292 and 0.405 with an average value of 0.361 ± 0.040.

The root density on the vertical soil profile was measured by counting every single root. The root diameter varied from 0.2 to 24 mm, whereas the number of roots per unit area ranged from 18 to 111 roots with an
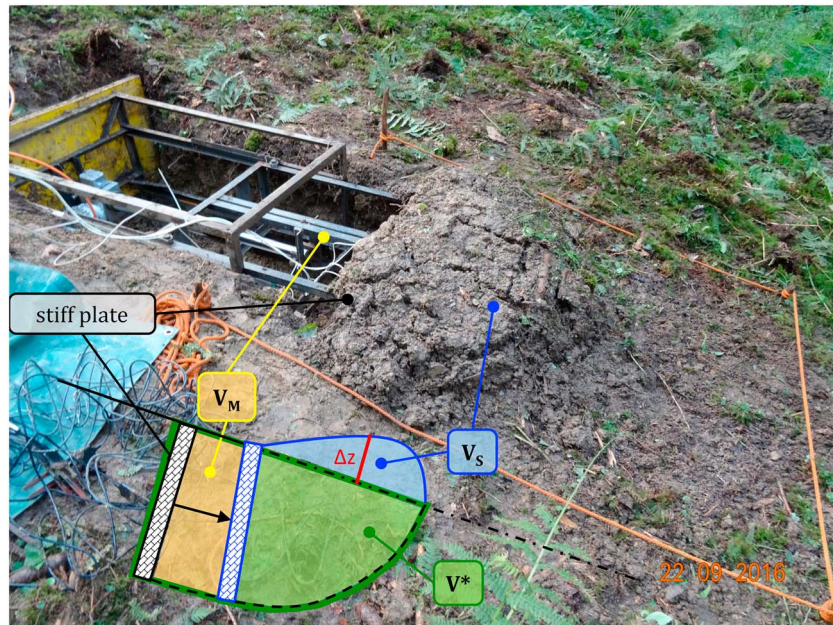
Figure 5. Photograph of one of the experiments at the end of the compression load and a schematic lateral view of the experiment. V^* is the unknown soil volume moved by the stiff plate, V_M is the moved soil volume, and V_S is the soil volume moved above the original ground surface.

average value of 40.27 ± 27.06. On average, two thirds of the roots belonged to the finer root diameter class (<1.5 mm).

The force measurements taken by the four load cells located on the four vertexes of the stiff plate were summed to provide the value of $F_{P\perp}$ exerted during the experiments. The corrections due to the frictional angle between the stiff steel plate and the compressed soil were almost negligible at approximately 2% of the measured values. The contribution of root reinforcement, however, strongly depends on the presence of roots, and the maximum estimated value of F_{rb-tot} was between 0.08 and 2.04 kN using Co-RBMw (equation (10)). Such force provided by the roots was deducted from F_{dyn}.

The observed behavior of the dynamic force as a function of displacement $F_{dyn}(\Delta x)$ showed a typical rapid increase until the maximum compression resistance is reached, which was followed by a moderate decline to a residual value (Figure 6a). This residual compression force represented a critical state in which the force remains constant while the displacement increases. The maximum values of F_{dyn} varied from 8.49 to 31.67 kN and occurred inside a range of Δx between 43.2 and 85.2 mm. If this displacement was normalized by H, it varied from 0.10 to 0.19 with an average value of 0.152 ± 0.026. The residual compression force ascended from 2.73 to 22.58 kN. Moreover, the measurements of soil moisture during the experiments indicated that θ_v increased up to the maximum passive earth force and slightly decreased to a residual constant value (Figure 6b).

4.2. Friction Between the Stiff Plate and Compressed Soil Wedge

As discussed in section 3.3.3.1, the upper bound of δ can be estimated by monitoring the inclination α of the compression machine during the experiment. The angle α varied from 1.80° to 8.90° from the control to the end of the experiment, with an average value of $5.41° \pm 2.08°$ (Figure 7). The angle δ assumed different values at the end of each pause, and its behavior was evidently inverse to the force-displacement curve. The lowest values of $\delta^{pause-2}$ occurred after $F_{P\perp}$ reached its peak (pause-2), whereas the higher values of δ^{res} occurred at the end of the experiment. Consequently, $\delta^{pause-2}$ ranged from $0.066\ \phi'$ to $0.344\ \phi'$ and presented an average value of $0.183\ \phi' \pm 0.080\ \phi'$, whereas δ^{end} reached a value from $0.178\ \phi'$ to $0.503\ \phi'$ with an average value of $0.324\ \phi' \pm 0.081\ \phi'$. Intermediate values were evaluated at the end of the first loading phase $\delta^{pause-1}$, with values between $0.084\ \phi'$ and $0.457\ \phi'$.
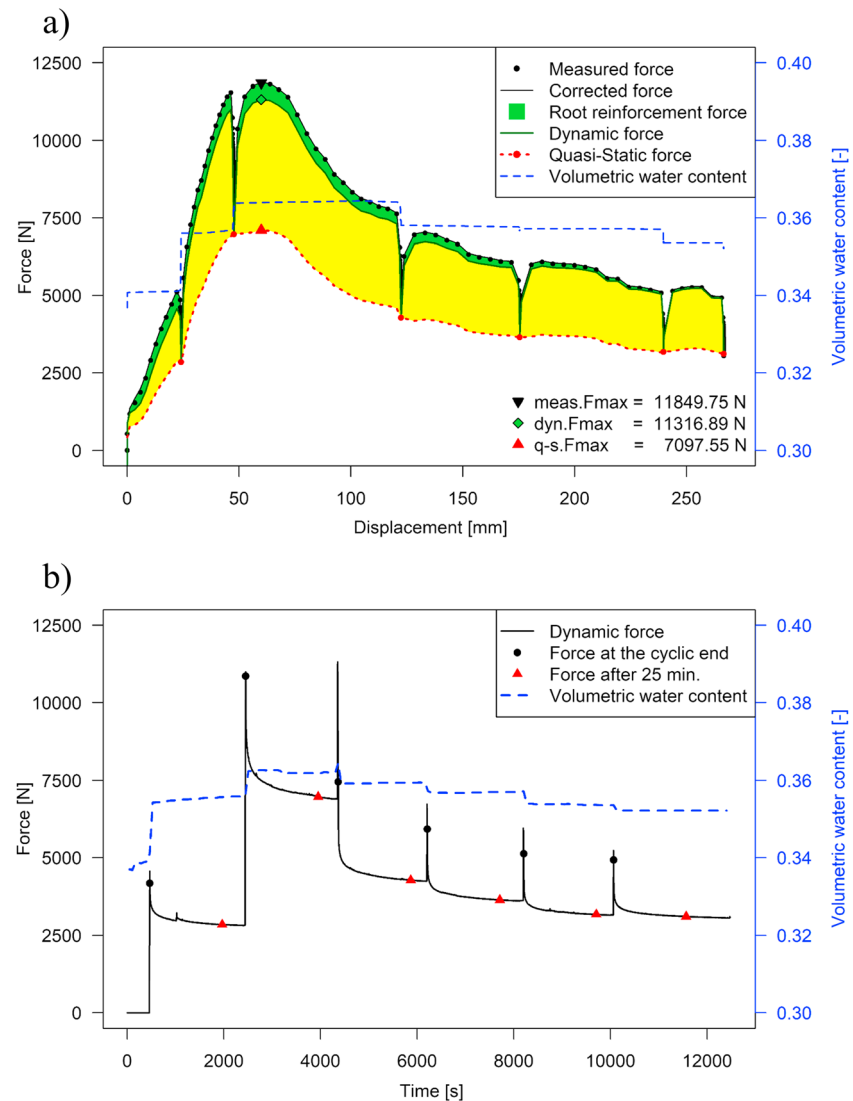
Figure 6. (a) Force as a function of displacement and (b) force as a function of time. A black circle shows the dynamic force before the pause, whereas a red triangle indicates the quasi-static force at the end of the pause.

4.3. Dynamic Versus Quasi-Static Force

The procedure applied to determine F_{q-s} consisted of fitting the decay of F_{dyn}^* (equation (15)) and estimating the asymptotic constant value Γ for each pause of every experiment (equation (16)), which approximately represents a quasi-static condition. Figure 8 demonstrates that a rapid decline of the compression force is clearly visible. The values of Γ indicated an evident difference between the two states and varied from 0.471 to 0.784, with an average value of 0.614 ± 0.071, as shown in the boxplot in Figure 8. The variability of Γ is large as shown by the presence of five outliers. They are, however, equally distributed on both sides of the boxplot. Additionally, Γ was individually evaluated for each experiment by taking the soil moisture condition into account (Figure 9). The first four tests were conducted under natural conditions, and the seven others were conducted under artificial soil moisture conditions due to the simulated rainfall. Figure 9 shows that Γ is 0.60 on average and presents moderate variability. However, exceptions were also evident. For example, experiment #05 was conducted on a rainy day and showed low Γ values, whereas during the second part of experiment #11, the steel structure of the compression machine nearly collapsed, which forced us to stop the test. Although several measurements under different soil moisture conditions were collected, no generalities could be made about the differences between the unsaturated and saturated
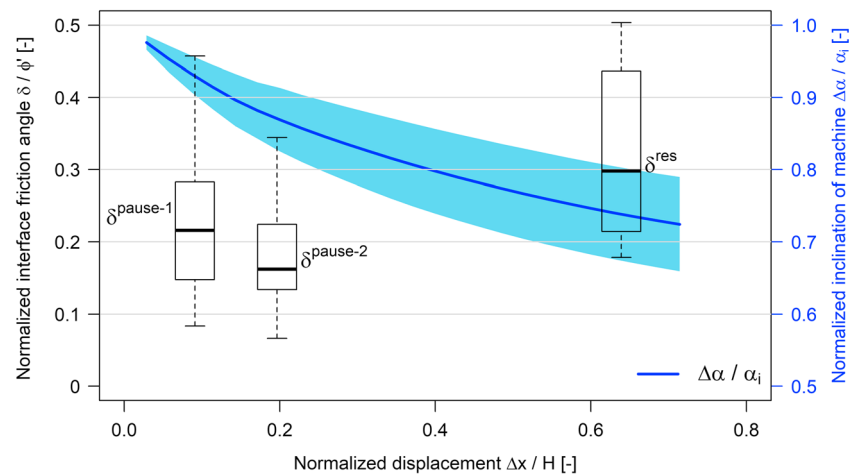
Figure 7. Normalized interfacial friction angle (box plots of δ/ϕ') as a function of normalized displacement ($\Delta x/H$) for pauses 1 and 2 and the residual state at the end of each experiment. The blue line is a regression of the normalized inclination of the compression machine $\Delta\alpha/\alpha_i$ as a function of the normalized displacement, with the light blue area corresponding to the 95% confidence interval of all experiments. Symbols are defined in the Notation section.

(i.e., after irrigation) conditions (Figure 8). F_{q-s} was evaluated by multiplying F_{dyn} per Γ, and its maximum values ranged from 5.61 to 24.55 kN as shown in Figure 10. Finally, the soil stiffness was evaluated as the ratio between the maximum F_{q-s} and the corresponding Δx. The soil stiffness varied from 0.094 to 0.310 kN/m and presented an average value of 0.171 ± 0.070 kN/mm, and it increased with increasing soil depth. Then, the experiments were grouped in three different classes, that is, 0.36–0.42, 0.42–0.46, and 0.46–0.50 m, and inside these classes, the soil stiffness had a small standard deviation and assumed average values equal to 0.107 ± 0.011, 0.207 ± 0.022, and 0.310 kN/mm, respectively.

A statistical analysis was performed to verify which factors influenced the maximum values of F_{q-s}. Kendall's τ was calculated to estimate a rank-based measure of association/correlation, whereas Pearson's r was calculated to measure the linear relationship between F_{q-s} and other external factors. These factors
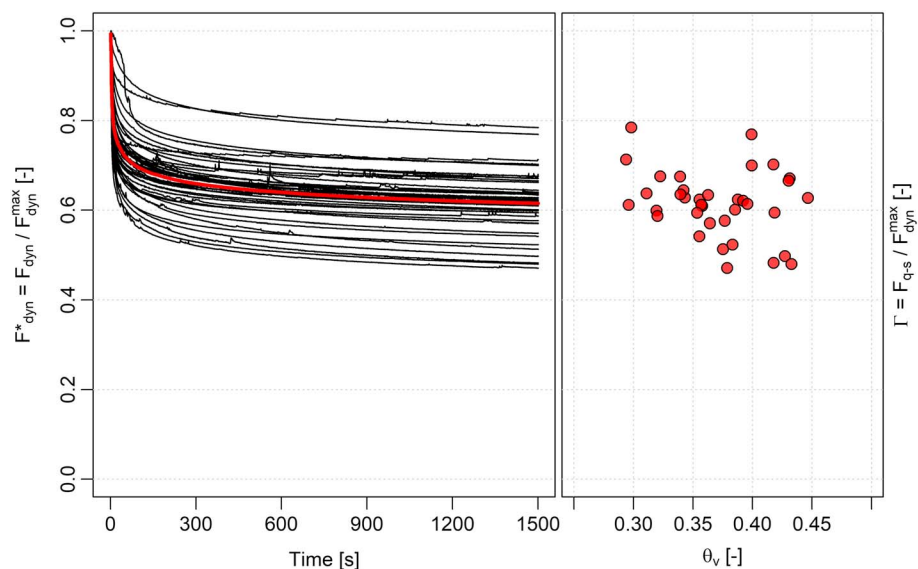

Figure 8. Normalized dynamic force F^*_{dyn} versus time during the 25-min pause. The red line represents the average value versus time for all experiments. The plot on the right displays the variability of Γ, which is the asymptotic values of the normalized dynamic force F^*_{dyn} as a function of the volumetric water content θ_v.

AGU
100
ADVANCING EARTH
AND SPACE SCIENCE

Journal of Geophysical Research: Earth Surface
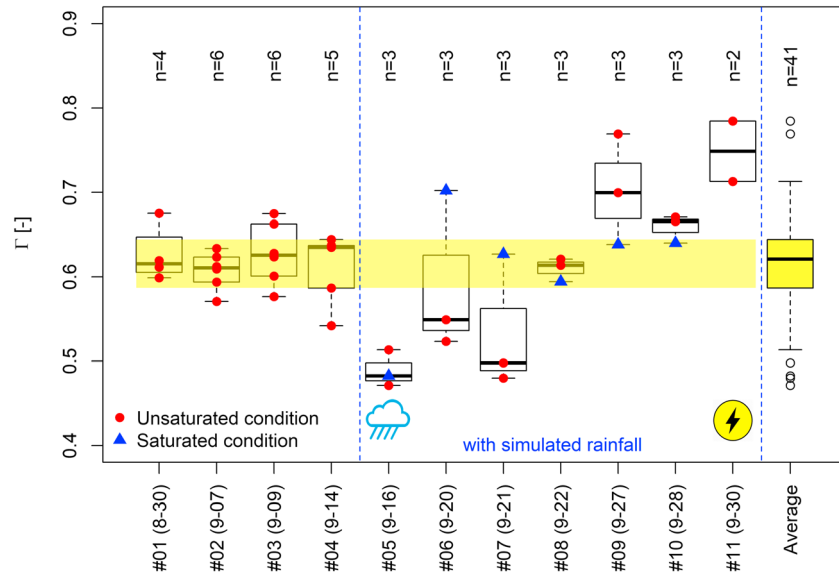
10.1029/2017JF004557

Figure 9. Evaluation of the ratio between the dynamic force at the end of the pause (i.e., quasi-static force) and maximum dynamic force denoted by Γ for the 11 experiments: four under natural soil moisture conditions and seven under artificial conditions influenced by the simulated rainfall. The yellow band represents the range in which 50% of the values are measured, the red circles indicate when the measurements were recorded for the unsaturated condition, and the blue triangles pinpoint the saturated condition after irrigation. The rainfall icon indicates that the experiment was conducted on a rainy day, whereas the thunder symbol indicates electrical problems with the equipment. On the right, the yellow box plot indicates the distribution of Γ values across all experiments.

were H, β, Δx and the normalized displacement at the maximum force Δx_{peak} and $\Delta x_{peak}/H$; θ_v at the control and the maximum compression force $\theta_{v\text{-starts}}$; and $\theta_{v\text{-peak}}$ and the difference between the inclination of the machine at control and at the end of the experiment $\Delta \alpha$. For these statistical analyses, all the samples need to be normally distributed. Therefore, Shapiro-Wilk tests were conducted (excluding experiment #11 [outlier data]) to verify the normal distribution. The statistics indicated that the maximum F_{q-s} correlated significantly with H ($r = 0.711$ and $\tau = 0.629$), moderately with β ($r = 0.407$ and $\tau = 0.225$), and weakly with Δx_{peak} ($r = 0.267$ and $\tau = 0.244$), $\Delta x_{peak}/H$ ($r = -0.079$ and $\tau = 0.111$), $\theta_{v\text{start}}$ ($r = 0.228$ and $\tau = 0.244$), $\theta_{v\text{-peak}}$ ($r = 0.254$ and $\tau = 0.289$), and $\Delta \alpha$ ($r = 0.134$ and $\tau = 0.111$).

4.4. Passive Earth Force Comparison

Two general formulations widely used in practice were selected to determine the maximum passive earth force per unit length, as previously described in section 2: gen-Rankine (equations (2) and (3)) and the log-spiral approach (equation (4)). The measurements were normalized by the plate width, and the differences between the observations and theories were estimated using two indicators: root mean square error (RMSE) and mean absolute percent error (MAPE). The comparison is shown in Figure 11. It is evident that the gen-Rankine provided the closest estimates and was the most accurate for this application. Additionally, no particular trend in terms of underestimation or overestimation was evident, and the performance indices assumed the lowest values (RMSE = 4.24 kN and MAPE = 26.77%). The log-spiral considerably overestimated the observations and yielded even greater values (RMSE = 16.46 kN and MAPE = 150.54%). Figure 11 also shows the range of the calculated values. Although the gen-Rankine provided the most accurate estimates, the values ranged between 7.48 and 13.44 kN, which were smaller than the observations. An extremely wide range (from 13.32 to 47.18 kN) was obtained for the log-spiral approach.
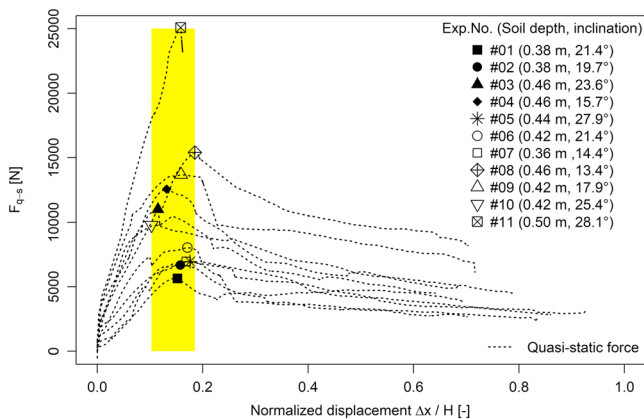

Figure 10. Quasi-static force F_{q-s} as a function of the normalized displacement $\Delta x/H$. The yellow area shows the range of displacement at the maximum compression force. Symbols are defined in the Notation section.
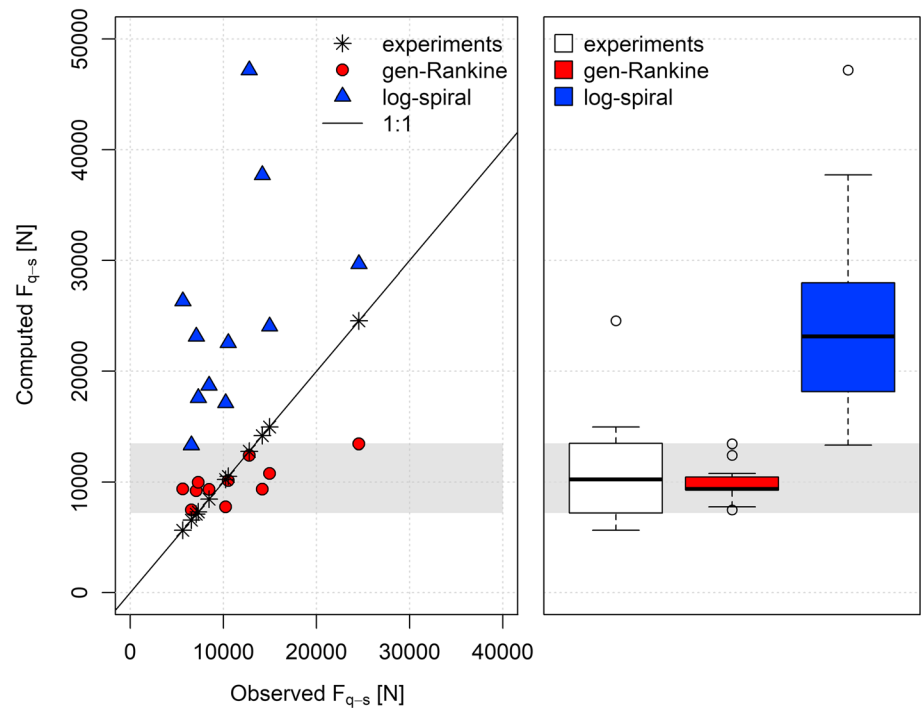
Figure 11. Comparison and variability between the observed measurements and theoretical calculations of $F_{q\text{-}s}$ for the gen-Rankine and log-spiral approaches. The gray band represents the range between the 25th and the 75th percentile of the observed values.
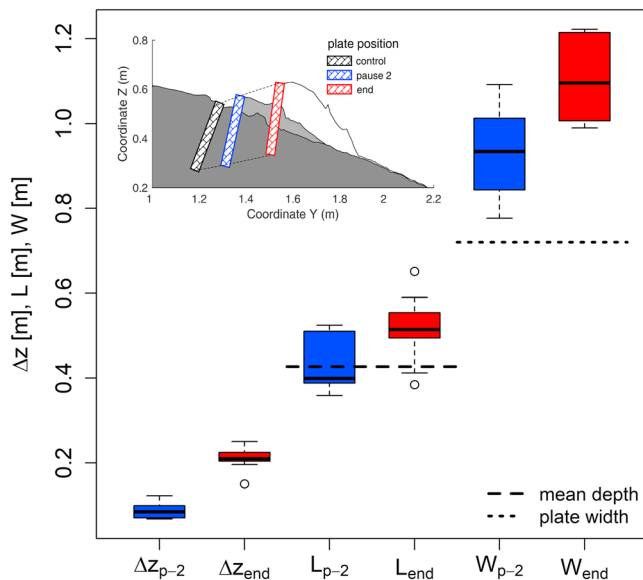

Figure 12. Box plots of 1-D geometrical measurements at two different stages: The subscript *p-2* corresponds to pause-2 and the subscript *end* corresponds to the final condition of the experiment. The inset shows an example of the postprocessing for experiment #01, where the dark gray, light gray, and white areas in the longitudinal profile represent the soil surface before the experiment, at pause-2 and at the end of the experiment, respectively, together with the position of the plate. Symbols are defined in the Notation section.

4.5. Geometry of the Compressed Wedge

The planar extension of the compressed wedge induced by the compression machine gradually varied with increasing Δx. The geometrical features were measured at two stages: at pause-2 (Figure 12) and at the end of the experiment (*end* in Figure 12). Δz ranged from 0.068 to 0.123 m, with an average value of 0.087 ± 0.018 m at pause-2 and increased to 0.150–0.250 m, with an average value of 0.209 ± 0.026 m. L ranged from 0.359 to 0.525 m at pause-2, which was approximately 11% more than H, and increased from 0.385 to 0.651 m until the end of the experiment. In terms of lateral expansion, W varied from 0.777 to 1.092 m at pause-2 and increased from 0.990 to 1.222 m. Figure 12 is an example of the postprocessing of three subsequent scans and shows six boxplots with the differences between the two stages for the three 1-D geometrical features. Concerning the behavior of the compressed wedge in terms of volume (3-D), the analysis clearly showed how the compressed wedge volume initially decreased and then expanded once the maximum resistance force was reached. As shown in Figure 13, ΔV_{3D} assumed negative values at pause-2 and varied between −0.013 and −0.001 m³, with an average of -0.004 ± 0.003 m³. However, at the end of the experiments, ΔV_{3D} had positive values ranging from 0.010 to 0.079 m³ that were one order of magnitude greater than the previous values, and it averaged 0.038 ± 0.021 m³.

4.6. Influence of Rainfall and Soil Water Content

Seven of the 11 experiments were performed under saturated conditions by using a rainfall simulator at a rate of 70 mm/hr for approximately 60 min after pause-2. For each experiment, a curve on the decline of the compressive force during pause-2 was fitted by the use of a three-
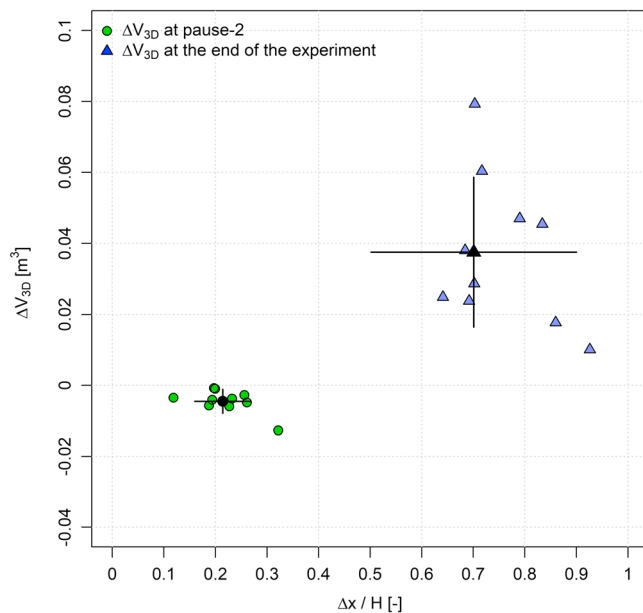
Figure 13. Three-dimensional geometrical characteristics of the compressed wedge ΔV_{3D} versus the normalized displacement $\Delta x/H$. Error bars show the standard deviation of the observations.

parameter negative exponential function (equation (15)). This function yielded an excellent fit with R^2 near unity and a RMSE of approximately 0.001. The fitted coefficients varied from −0.12 to 1.33 for Λ, −0.17 to 0.12 for Π, and −0.36 to 0.95 for Γ. For each experiment, all F^*_{dyn} fitted curves are shown in red lines in Figure 14 as a function of time. This procedure could be used to describe the decline of the compression force and assess the rainfall effects by comparing the fitted curves with the measurements under irrigation (black points in Figure 14). Furthermore, their maximum difference was calculated and called Ω hereafter. The average value of Ω was −10.04% ± 3.72%, with the exception of experiment #05, which was conducted during a natural rainfall event and therefore the initial soil water content was already high prior to irrigation. Thus, the estimated Ω in experiment #05 was −25.60%. Interestingly, the curves declined remarkably at approximately 11–12 min after initial irrigation with the exception of experiment #05.

5. Discussion

5.1. Experimental Measurements

The present study showed the results of specific and innovative field experiments performed to measure the passive earth force acting on cohesive forested soil and simultaneously monitor multiple factors, including soil moisture and compression plate movement (i.e., displacement and inclination) under different site conditions (i.e., soil depth and hillslope inclination). The main achievement was a load-displacement curve, which provided the magnitude of passive earth force that resists the movement of a failure soil mass as a function of the direction in which it moves. Few studies on force-displacement have been conducted at different scales and site characteristics (Duncan & Mokwa, 2001; Fang et al., 1994, 1997, 2002; Rollins & Cole, 2006; Wilson & Elgamal, 2010), which makes the comparison of data difficult. The observed curves were similar in all experiments despite wide differences in terms of peak compression forces (Figure 10). The shape is comparable to the results obtained for dense soils in other experiments. For example, Fang et al. (2002) investigated the differences in terms of magnitude and behavior under compression between sands with different densities. Their experimental setup consisted of a retaining wall that was 1.00-m wide and 0.55-m high and movable stiff plate that was 0.12-m thick as used in previous studies (Fang et al., 1994, 1997). Their results showed similar behavior for medium-dense and dense sand; however, they found that the mobilization of the maximum compression resistance occurred at a displacement between 0.015 and 0.030 $\Delta x/H$. This range of displacement is an order of magnitude smaller than that obtained in the presented experiments.

Wilson and Elgamal (2010) conducted another interesting experiment that is described in detail in Wilson (2009). To account for the contribution of the passive earth resistance against excessive displacement occurring along bridge abutments and piles, they measured force-displacement behind a 1.70-m-high vertical wall section inside a wider container filled with dense well-graded silty sand. The passive earth force increased with increasing displacement until reaching a maximum value of 0.035 $\Delta x/H$, followed by a slight decrease to a residual state, which occurred in the present study as well.

Gutberlet et al. (2013) provided similar results exploring the differences in terms of passive earth forces, analyzing different sands and combinations of them. As a matter of fact, they used a sandbox with a movable 0.225-m-high wall on one side that moved against the soil driven by an electric step motor. They clearly recorded a peak in compression force for dense materials and observed that the complete mobilization required a displacement of 0.02 $\Delta x/H$ for quartz sand and 0.05 $\Delta x/H$ for crushed gabbro. Mixing the two materials showed that mobilization always occurred within this range of displacement.

Askarinejad et al. (2018) conducted a full-scale landslide-triggering experiment on a natural sandy slope near the village of Rüdlingen (Canton of Schaffhausen, Switzerland) to determine the precursors of soil instability, and they monitored the horizontal earth pressure using three pressure transducers pushed into the soil at 0.60 m of depth and positioned in different zones of the test site during the triggering
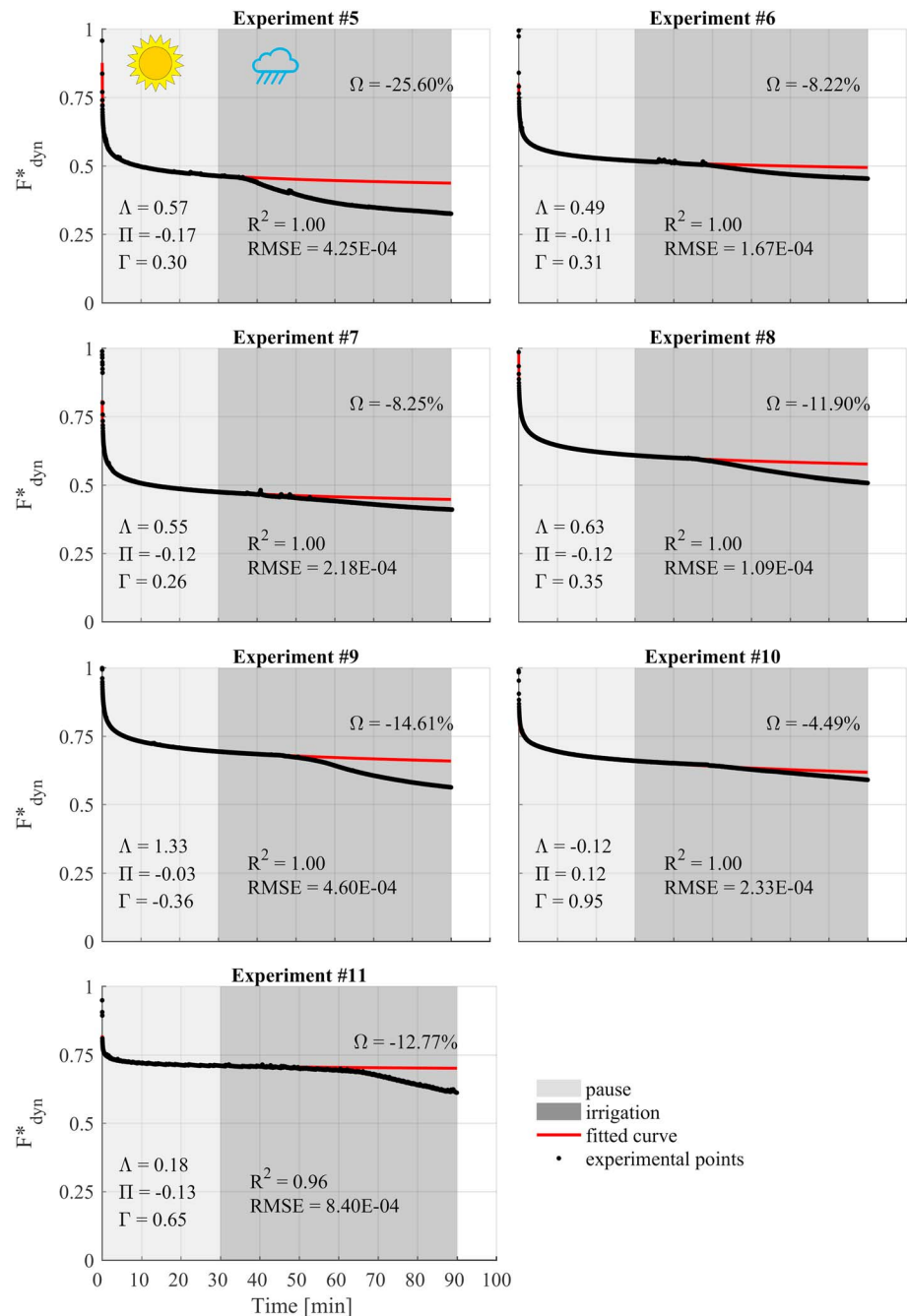
Figure 14. Decline of the dimensionless dynamic compression force F^*_{dyn} during pause-2 and simulated rainfall. The black points represent the measured values, the red line is the fitted curve before irrigation, the light gray area corresponds to the dry soil condition, and the gray area corresponds to the saturated condition. Ω is the difference between the fitted curve and the measurements; Λ, Π, and Γ are the coefficients of the three-parameter negative exponential function (15); and the coefficient of determination R^2 and root-mean-square error (RMSE) are the performance indices of the fit.

mechanism caused by an artificial rainfall. The maximum horizontal passive earth pressures varied from 12.30 to 33.55 kPa, which approximately correspond to forces ranging between 3.50 and 10.10 kN. A comparison with the observations in the present study and a consideration of different soils showed that the measurements were of the same order of magnitude.
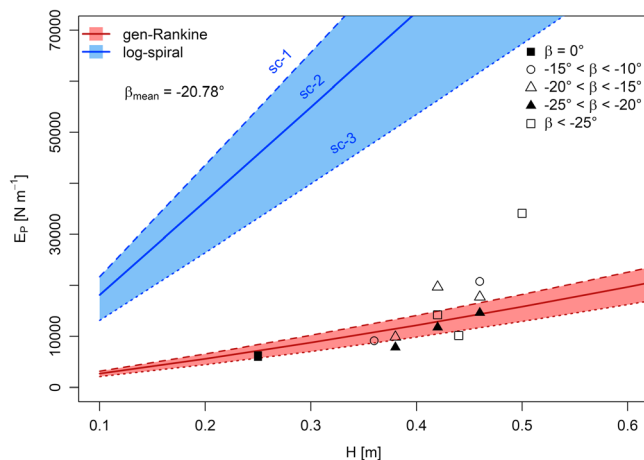
Figure 15. Passive earth force at different soil depths. Symbols indicate the measured quasi-static forces during experiments in the field (this study) and the laboratory (Schwarz et al., 2015). The colored bands represent theoretical calculations for the gen-Rankine and log-spiral approaches, whereas the different line types indicate different soil water contents (sc-1, sc-2, and sc-3 as described in detail in Table 2) and therefore different values of internal friction angle and soil cohesion, with a fixed inclination equal to −20.78°, which corresponds to the average of those measured during the field experiments.

With respect to displacement at peak compression, Schwarz et al. (2015) measured similar values in laboratory experiments using the same soil material used in this study. However, their force-displacement curve showed a continuous increase of force with no peak value, which was probably due to the different laboratory setups between their experiments and those presented here: in the experimentation by Schwarz et al. (2015), the soil was confined in a box, which was not performed here, and the compression plate movement was horizontal.

Moreover, the obtained force-displacement curves confirmed that the soil stiffness substantially depends on the soil depth (Terzaghi et al., 1996). Figure 10 shows that the soil stiffness, which was evaluated as the ratio between the maximum compression resistance and the mobilized displacement, increased with increasing soil depth classes. This study is consistent with that of Wilson and Elgamal (2010), who conducted numerical and experimental studies on different types of backfilled soils and showed an extensive range of variation of soil stiffness as a function of soil depth.

5.2. Measured Passive Earth Force Versus Theoretical Calculations

The comparison between the quasi-static measurements of the maximum passive earth force and the theoretical calculations showed that the gen-Rankine method provided the most accurate and consistent values. However, this theoretical approach estimated a small range of values for the combinations of depth and hillslope inclination tested in the field and underestimated the compression earth force with increasing soil depth as shown in Figure 11. Alternately, the log-spiral approach yielded generally larger values, approximately 1.51 times larger than the measured ones.

These discrepancies between observed and predicted values can be attributed to the soil characteristics at the study site. Specifically, the experiments were conducted on a particular forested soil classified as clayey gravel according to the Unified Soil Classification System soil classification, and it presents high cohesion (i.e., c' 15 kPa) and a low friction angle value (i.e., ϕ' 24°). The site's soil characteristics increase the difficulty of comparing the results with that of other studies because of the lack of observations on clay soils under compression. In the literature, almost all experiments were conducted on granular soils under artificial conditions, i.e., in the laboratory (e.g., Terzaghi, 1920). Most studies indicated that the gen-Rankine approach generally underestimates the passive earth resistance while the log-spiral approach produces a slight overestimation (Bowles, 1997; Duncan & Mokwa, 2001; Fang et al., 1994, 1997; Narain et al., 1969). Especially for dense sands, the log-spiral approach provided good estimates of the compression resistance peak (Fang et al., 2002; Wilson & Elgamal, 2010). Most studies considered the log-spiral approach to be more accurate than other methods because it exceeded the assumption of the planar sliding surface of Rankine's theory, which suggested a nonlinearity. Unfortunately, this fact could not be confirmed because no evidence of failure or shear band was found despite the careful excavation of the failure wedge after each experiment.
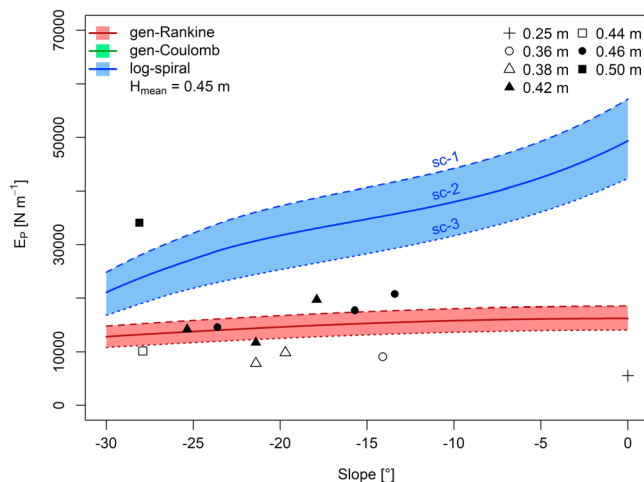

Figure 16. Passive earth force at different inclinations of backfill. Symbols indicate the measured quasi-static forces during experiments in the field (this study), whereas the colored bands represent the theoretical calculations for the gen-Rankine and log-spiral approaches. The different line types indicate different soil water contents (sc-1, sc-2, and sc-3 as described in detail in Table 2) and therefore different values of internal friction angle and soil cohesion, with a fixed depth of 0.45 m, which corresponds to the average of those measured during the field experiments.

Alternately, the presented observations are with the theoretical calculations show a strong relationship between maximum passive earth force and soil depth as shown in Figure 15 and as achieved by the statistical analysis, which revealed the highest values of correlation indices ($r = 0.711$, and $\tau = 0.629$). Conversely, a lower correlation was exhibited between maximum passive earth force and hillslope inclination ($r = 0.407$, and $\tau = 0.225$). This finding indicates that the range of backfill inclination is one of the most critical factors of the theoretical calculations.

In Figure 16, the calculation of E_P as a function of β using the selected theories and the same set of input parameters is shown. The gen-Rankine's calculations have a symmetrical behavior with respect to the longitudinal axis: whether the backfill inclination is $-30°$ or $+30°$, the passive earth resistance assumes the same value. This fact is clearly incorrect for positive values of β, whereas it is feasible for negative values (e.g., Bowles, 1997; Fang et al., 1997). In addition, the gen-Rankine's formulation imposes a significant restriction, because it does not consider the wall inclination, that is, it neglects the inclination of downslope face. Considering only the negative values of β, a further critical condition occurs when the soil is cohesionless and the backfill inclination is steeper than the internal friction angle. The gen-Rankine's K_P becomes a complex number when the cohesion term is not high enough to impede that the square root term in equation (2) assumes a negative value. A similar problem afflicts the log-spiral approach: $K_{P\gamma}$ becomes indeterminate when $\beta > \phi'$ because the log-spiral slip surface degenerates to a planar surface with radii approaching infinity and violates the optimization constraints.

For this reason, Soubra and Macuh (2002) suggested reasonable practical limitations, particularly for the case of cohesionless soils, for obtaining $K_{P\gamma}$ values similar to those proposed into the tables proposed by Caquot and Kérisel (1948) and readjusted by Kérisel and Absi (1990), i.e., $\phi' \leq 40°$, $1/3 \leq \delta/\phi' \leq 2/3$, $\beta/\phi' \leq 1/3$ and $\lambda = 0°$. This problem is partially reduced by considering the soil cohesion in equations (2) and (4), even if Macuh and Škrabl (2010) verified that K_{Pc} values are not admissible if obtained by applying the basic corresponding state theorem (equation (A14)) developed by Caquot (1934). Therefore, within this state of the art, the applicability of such formulations seems to be limited in the landslide model for assessing the slope stability over natural landscapes. Conversely, the presented modifications show their application for a real site (i.e., this study area) considering a reasonable range of soil depth and slope inclination (Figures 15 and 16). Additionally, these investigations highlight how the gen-Rankine method and the log-spiral approach are not accurate based on comparisons of the measurements (Figure 11). Nevertheless, because the observations mostly fell between the gen-Rankine and the log-spiral calculations, the two theories actually provide the lower and upper bounds of the passive earth force with the exception of five cases in which the passive earth forces were lower than the calculated values.

5.3. Implications of 3-D Edges

Quantifying the effects of the 3-D edges on the measured compression force is arduous and challenging, in particular because of the difficulty in finding field evidence of the 3-D failure mechanism. The strain localization of deformations was not evident within the soil mass involved in the experiments, and the lack of such an indication inhibited our ability to measure and model the shear band propagation as expected. Moreover, few scientific contributions have dealt with this issue, and none of them investigated soils with similar characteristics to those of the study site. Nevertheless, measuring the extension of the soil surface involved in the failure could highlight differences with other studies. A comparison of the measurements with those obtained by Capilleri et al. (2015), who tested siliceous sand at a similar scale but in the laboratory, shows that similar extensions for the length of the failure wedge occurred while significant differences for the width occurred. In fact, Capilleri et al. (2015) showed that the measured width was approximately consistent with the extension of the plate, whereas the measured width was significantly greater in this study. This different behavior probably depends on the soil granular composition.

Although field findings did not adequately explain the implications of the 3-D effects, the theoretical calculation using equation (5) can approximate such a quantification. If the equation was corrected by fixing an average value of the shape parameter $C = 0.52$ as proposed by Regenass et al. (2000), then the yield values of the compression force would be approximately 30% greater, that is, the passive earth pressure coefficients ratio K_{P-3D}/K_{P-2D} is 1.3 considering a B/H of $\cong 1.9$.

This estimate was not too far from those obtained by other numerical simulations. For example, Benmebarek et al. (2008) estimated a value of this ratio that was twice as high for $B/H \leq 1$ and at unity for $B/H \gg 10$, whereas Capilleri et al. (2015) estimated a value of 1.5 for $B/H = 2$.

5.4. Friction Between the Plate and Compressed Soil Wedge

The presented estimates of the friction angle between the stiff plate and the soil showed an inverse dependence with respect to the expected compression resistance, which is consistent with Rowe and Peaker

(1965) and Narain et al. (1969). Indeed, these authors suggested that the wall friction angle changes with the displacement and is mainly dependent on the instantaneous direction of wall displacement at each stage of deformation. In addition, Sherif et al. (1982) indicated that the maximum wall friction does not occur simultaneously with the maximum shearing resistance along the rupture surface. Although this factor is fundamental for a reliable estimate of passive resistance, only a few studies have focused on quantifying the interface friction during a compression test. Potyondy (1961) conducted interface shear tests on a variety of structural materials and soils, obtaining a wide range of values. For the interface between steel and soil, the typical maximum value of δ ranged from 11° to 22° (Bowles, 1997; Duncan & Mokwa, 2001) and was comparable to the observations at the end of the experiment. Moreover, the movement of the plate during the experiment was consistent with a large-scale experiment (Bozorgzadeh et al., 2008) and with numerical analysis (Shiau et al., 2008). The first study investigated the response of bridge abutments in the longitudinal direction and observed a significant nonlinear behavior of the force as a function of horizontal displacement and a slight vertical movement controlled by the properties of the soil-structure interface. The second work examined the passive earth resistance using the finite element formulations and showed that the directions of the velocity for each finite element were comparable with the presented results. However, the quantification of $\delta^{pause-2}$ showed a slight impact on the results, with an increase of approximately 2% of the measured compression force. Thus, these results underlined that the passive earth force was strongly dominated by the effects of soil-soil friction and how values greater than 0.4–0.5 times ϕ' yield an overestimation of E_P computed using Coulomb's theory, as already indicated by several authors (Duncan & Mokwa, 2001; Morgenstern & Eisenstein, 1970).

5.5. Dynamic Versus Quasi-Static Forces

An evaluation of both F_{dyn} and the quasi-static force F_{q-s} can increase our knowledge of how much of these forces are activated during the compression phase occurring at the toe of a shallow landslide during its failure as well as the underlying mechanisms. The soil mass undergoes an acceleration that generally starts under a quasi-static condition and reaches a velocity up to 1 m/s (Cruden & Varnes, 1996). The magnitude and timing of the activated passive earth force are determinant to define if a potential landslide mass runs out or stops at the toe. In the present study, the results showed a clear variation between F_{dyn}, which occurs when the soil mass is moving, and F_{q-s}, which occurs when the soil mass is in a state of stable equilibrium. The difference between the two is considerable (F_{dyn} is approximately 40% larger than F_{q-s}), and it is consistent with the measurements of Schwarz et al. (2015). F_{dyn} was completely activated at low displacement of approximately 15% of H, although it rapidly decreased once the displacement stopped (the first loading step). The observations clearly showed the decay of compression force corresponding to the dissipation of excess pore pressure and the variation of the rheological properties of soil (Ghezzehei & Or, 2001, 2003), notwithstanding the short time between the loading phases. This process implies both the mobilization of the passive earth force and the force redistribution on a slope, and these factors have to be quantified and integrated into numerical models; moreover, better results are obtained if these factors are related to another variable, such as the volumetric strain rate or the displacement (Cohen & Schwarz, 2017). Indeed, the interplay between the displacement rate and changes in suction and pore water pressure at the toe of the landslide determine the development of the failure. In the case of a soil with an initial relatively low water content, deformation is slow and the pore water pressure/suction at the moment of maximum passive earth force mobilization is low, resulting in an arrest of the sliding mass. Conversely, if the soil already has a high soil water content, it can be subject to a rapid increase of soil moisture and therefore pore water pressure before the dilatation phase along the failure surface due to rainfall events. Furthermore, the dissipation of excess pore water pressure occurs until a steady state is reached, and the increase of connectivity of water-saturated pores causes a reduction of the soil shear resistance along the slip surface, which leads to failure. This conceptualization is well documented by several studies (Askarinejad et al., 2012, 2018; Lehmann et al., 2013).

5.6. Effects of Soil Water Content

Passive earth force strongly depends on soil properties, soil depth, and hillslope inclination as well as on soil moisture as emphasized by the study of Poterasu (2013), who investigated this aspect in detail through compression experiments on fractions of Kaolin clay content (6% to 10%). Poterasu (2013) showed that the behavior of passive earth force was associated with pore volume saturation ranging from 5% to 100%. This study

highlighted that the collapsing mechanisms of the clay-water bridges between the grains of the granular material were responsible for a significant reduction in soil stiffness and strength. Because the range of soil moisture in the experiments of this study was limited ($\theta_v = 0.292$–0.405), a relationship between the volumetric water content and maximum quasi-static compression force was not found as shown by the correlation analysis ($r < 0.254$ and $\tau < 0.289$). However, this range of soil water content, which corresponds to a range of saturation degree between 0.70 and 0.90, represents the most critical condition leading to the failure as verified in laboratory experiments (see Schwarz et al., 2015). In addition, the presented observations enabled the monitoring of the behavior of soil water content starting from a high value, during the compression phase. The soil moisture increased while the compression force increased, and both measurements approximately reached their maximum values at the same time, which was probably due to the reduction of pore volume and the increase of pore pressure. This evidence was also highlighted in the study conducted by Iverson et al. (2000), who explained that the contraction associated with aggregate crushing is likely the main cause of excess pore pressure and responsible for soil weakening and landslide acceleration. Concerning the effects of rainfall, statistical analyses performed on the data set of the seven field experiments with simulated rainfall did not yield a strong correlation between the variation of soil moisture condition and the measured maximum resistant force or variation from dynamic to quasi-static state. However, in terms of timing of the hydrological process, the initial water content influenced the decline of F_{dyn} during the simulated rainfall (Figure 14). For example, experiment #05 showed a remarkable decline shortly after the beginning of irrigation, whereas the other experiments displayed a decline only after several minutes. Moreover, rainfall intensity and initial pore water pressure inside the subsoil affected this hydrological behavior and, as shown in the experimental results, they affected the measurements of passive earth resistance as well.

5.7. Implications for Slope Stability Analysis

Despite the continued efforts to improve our knowledge regarding the mechanical transformation of soil structures, the evolution of soil hydraulic processes, and rheological dynamics during landslide events, the spatiotemporal heterogeneity of rooted soil creates enormous difficulties for characterizing large areas. Although many studies have proposed and developed a wide range of slope stability analyses tested through laboratory or field experiments (Bordoni et al., 2015; Iverson, 2000; Lehmann et al., 2013), several aspects on the evolution of soil-stress configuration remain unclear.

The present study is an integral part of the modeling development process started by the pioneering work of Burroughs (1985) and provides empirical evidence about (i) the role of soil displacement, (ii) the magnitude of soil resistance under compression, and (iii) the soil mass involved under compression.

Field experiments have generated measurements of passive earth force that are fundamental for calibrating 3-D force-balance models and selecting appropriate geotechnical formulations for determining K_P. Moreover, these analyses quantify the evolution of compressional forces as a function of soil displacement and allow for an examination of limitations in the equilibrium approach. For example, the assumption of a rigid sliding block implies that ultimate states of active and passive forces act simultaneously. To overcome such limitations, the role of soil displacement becomes crucial, and including this factor requires consideration of the timing of when earth forces are actively applied to the sliding soil mass, which may improve the results as shown in Askarinejad et al. (2012, 2018) and later in Cohen and Schwarz (2017). For more details, see Text S2 in the supporting information.

Additionally, this work may contribute to solving landslide pressure problems and improving models that simulate thrust faults in areas of compression. For example, Savage and Smith (1986) proposed an application of the Mohr-Coulomb theory through an integration of hyperbolic differential equations for stress and velocity fields in a 1-D semi-infinite space. Their model predicted longitudinal tensile stresses at the upper part of the soil mass and compression stresses at the toe of the unstable mass. Furthermore, Savage and Wasowski (2006) validated the model on a real case in Southern Italy. Sdao and Simeone (2007) and later Doglioni et al. (2011) developed a simple analytical model of the passive force at the toe of a landslide based on the Mohr-Coulomb criteria, representing the stress state for an infinite slope model. Their model evaluated the contribution of the strength at the toe, the shape of the backward passive failure surface, and the maximum longitudinal dimension of the landslide with the aim of understanding the evolution of the

landslide mechanism. Within the context of the above models, the observations provide additional information related to compression force measurements both in terms of the nonlinear behavior of the displacement and the soil mass involved with the displacement. Improving the knowledge of the evolution phase subsequent to a soil mass acceleration may lead to better analysis and prediction of the progressive failure caused by the passive toe failure. Indeed, hillslope failures often take place along a slip surface with reduced strength and progressively move downslope as long as the driving component of the gravity force is approximately in equilibrium with the compressive earth resistance (Savage & Smith, 1986; Sdao & Simeone, 2007). When the compression stresses at the bottom of the sliding soil mass exceed the maximum passive earth strength, the triggering mechanism reactivates, potentially causing intense acceleration as in the case of creeping and constrained landslides (Oberender & Puzrin, 2016; Puzrin & Schmid, 2012; Puzrin & Sterba, 2006). Moreover, the failure at the bottom of the sliding layer surely affects the kinematics of the landslide (Friedli et al., 2017).

In this study, the results can also be used to inform requisite resolutions for digital terrain models of hillslope stability (e.g., Penna et al., 2014; Tarolli & Tarboton, 2006), which are rapidly advancing with the development of remote sensing technologies for mapping and analyzing surface topography. In particular, the 1-D and 3-D characterizations of compressed wedge geometry can guide the requisite discretization of the landscape for characterizing failure processes. Although the measurements did not detect a clear sliding failure surface or a shear zone, the 1-D characterization showed that the planar size of the compressed wedge was of the same order of magnitude as the soil depth as suggested by several authors (Capilleri et al., 2015; Fang et al., 1994; Wilson & Elgamal, 2010). Therefore, in the case of finite volume methods, the resolution of the digital terrain discretization should be at least as large as the expected depth of the sliding surface.

6. Summary

Passive earth force is an important element of slope stability analyses; however, it has been poorly studied in natural settings, and the applicability of existing geotechnical approaches for predicting passive earth forces in such environments is uncertain. To address these issues, field measurements were conducted using specially designed experimental equipment on a clayey gravel soil in a coniferous forest site susceptible to shallow landslides. In the present study, the measurements clearly showed that the behavior of the compression force during the experiment was a function of several factors, the most important of which was the soil depth, although the dynamics of loading, soil properties, backfill inclination, and change in soil water content also had relevant impacts on the compression force. Additionally, these results highlighted the following:

1. The force-displacement curves assumed identical shapes in which an initial increase occurred until reaching a maximum compression force and then a decrease occurred to a residual compressive state;
2. The maximum dynamic compression force varied from 8.49 to 31.67 kN for clayey gravel soils with different combinations of soil depths (0.38–0.50 m) and slope inclinations (13.4°–28.1°);
3. The quasi-static compression forces were approximately 38.6% lower than the dynamic forces, and the maximum values varied from 5.61 to 24.55 kN;
4. A comparison of the observations of passive earth forces with theoretical calculations showed that gen-Rankine's theory provided the most accurate predictions while the log-spiral approach provided considerably overestimated values;
5. The effects of rainfall on the quasi-static compression force caused a decrease of the resistance by approximately 10% under an initial average soil moisture of 36%;
6. The downslope wedge initially compressed itself until failure, and then dilatancy and visible cracks on the surface occurred, with subsequent volume expansion.

Notation

E_P Passive earth force (N/m)
γ Unit weight of soil (KN/m)
c' Soil effective cohesion (Pa)

c	Soil cohesion (Pa)
ϕ'	Internal friction angle of soil (rad)
β	Backfill inclination (rad)
δ	Frictional interaction angle between wall and soil (rad)
λ	Angle of the internal face between wall and vertical direction (rad)
H	Soil depth (m)
q	Vertical surcharge loading (KN/m^3)
K_P	2-D coefficient of passive earth pressure (−)
$K_{P\gamma}$	Coefficients of passive earth pressure due to soil weight (−)
K_{Pc}	Coefficients of passive earth pressure due to soil cohesion (−)
K_{Pq}	Coefficients of passive earth pressure due to surcharge (−)
B	Width of plate (m)
$K_{P\text{-3D}}$	3-D coefficient of passive earth pressure (−)
C	Shape factor for evaluating $K_{P\text{-3D}}$ (−)
θ_v	Volumetric water content (m^3/m^3)
Δx	Displacement (mm)
$F_{P\perp}$	Measured compression force perpendicular to the plate (N)
W_{CM}	Weight of the compression machine with one side on the ground (N)
α	Inclination of compression machine (rad)
$\Delta\alpha$	Difference between inclination of machine at control and at the end of experiment (rad)
F_P	Measured compression force (N)
F_{rb}^{ult}	Maximum buckling-tensile force (N)
ϕ	Root diameter (mm)
ξ	Empirical exponent of F_{rb}^{ult}-ϕ curve (−)
F_0	Multiplicative coefficient of F_{rb}^{ult}-ϕ curve (−)
$F_{rb\text{-}i}$	Contribution of root diameter class i to root reinforcement under compression (N)
$F_{rb\text{-}tot}$	Root reinforcement under compression (N)
N_i	Number of roots in diameter class i (−)
n_c	Number of diameter class (−)
Δx^*	Normalized displacement than that measured at maximum value of compression force (−)
S	Survival function (−)
k	Spring constant function (−)
k_i	Intercept of spring constant function (−)
k_p	Multiplicative coefficient of spring constant function (mm^{-1})
σ	Scale Weibull parameter (−)
ω	Shape Weibull parameter (−)
F_{dyn}	Dynamic compression force (N)
F_{dyn}^*	Dynamic compression force at end of loading step (N) normalized for its maximum value
$F_{q\text{-}s}$	Quasi-static compression force (N)
t	Time (s)
Λ	Empirical coefficient of equation (15) (−)
Π	Empirical exponent of equation (15) (−)
Γ	Asymptotic value of equation (15) corresponding to the ratio of quasi-static and maximum dynamic compressional forces (−)
L	Length of compressed wedge (m)
W	Width of compressed wedge (m)
Δz	Height of compressed wedge (m)
ΔV_{3D}	Volumetric difference (m^3)
V^*	Soil volume subject to passive earth pressure (m^3)
V_M	Soil volume moved by stiff plate (m^3)
V_S	Soil surface volume difference (m^3)
r	Pearson correlation coefficient (−)
τ	Kendall rank correlation coefficient (−)

Appendix A

Appendix A reports the equations for the log-spiral approach developed by Soubra and Macuh (2002) for sloping backfill including friction and cohesion strength in detail. The definitions of terms are reported in the Notation section

$$K_{P\gamma} = \frac{2}{\left(\frac{l}{r_0}\right)^2} \frac{f_1 - f_2 - f_3}{g_4} \tag{A1}$$

$$K_{Pq} = \frac{1}{\frac{l}{r_0}} \frac{f_6}{f_4} \tag{A2}$$

$$K_{Pc} = \frac{1}{\frac{l}{r_0}} \frac{f_7 - f_5}{f_4} \tag{A3}$$

$$f_1 = -\left\{ \frac{e^{3(\theta_1 - \theta_0)\tan(\phi')}\left[3\tan(\phi')\sin(\theta_1) - \cos(\theta_1)\right] - 3\tan(\phi')\sin(\theta_0) + \cos(\theta_0)}{3\left[9\tan^2(\phi')\right]} \right\} \tag{A4}$$

$$f_2 = \frac{1}{6}\frac{L}{r_0}\left[2\sin(\theta_0) - 2\frac{l}{r_0}\sin(\sigma) + \frac{L}{r_0}\cos(\beta)\right]\cos(\theta_1 - \beta)e^{(\theta_1 - \theta_0)\tan(\phi')} \tag{A5}$$

$$f_3 = -\frac{1}{6}\frac{l}{r_0}\sin(\theta_0 - \sigma)\left[2\sin(\theta_0) - \frac{l}{r_0}\sin(\sigma)\right] \tag{A6}$$

$$g_4 = \cos(\delta - \sigma)\left[\cos(\theta_0) - \frac{1}{3}\frac{l}{r_0}\cos(\sigma)\right] - \sin(\delta - \sigma)\left[\sin(\theta_0) - \frac{1}{3}\frac{l}{r_0}\sin(\sigma)\right] \tag{A7}$$

$$f_4 = \cos(\delta - \sigma)\left[\cos(\theta_0) - \frac{1}{2}\frac{l}{r_0}\cos(\sigma)\right] - \sin(\delta - \sigma)\left[\sin(\theta_0) - \frac{1}{2}\frac{l}{r_0}\sin(\sigma)\right] \tag{A8}$$

$$f_5 = \frac{l}{r_0}\frac{\tan(\delta)}{\tan(\phi')}\sin(\sigma - \theta_0) \tag{A9}$$

$$f_6 = \frac{L}{r_0}\left[-\sin(\theta_0) + \frac{l}{r_0}\sin(\sigma) - \frac{1}{2}\frac{L}{r_0}\cos(\beta)\right] \tag{A10}$$

$$f_7 = \frac{1}{2\tan(\phi')}\left[e^{2(\theta_1 - \theta_0)\tan(\phi')} - 1\right] \tag{A11}$$

where

$$\frac{l}{r_0} = -\frac{e^{(\theta_1 - \theta_0)\tan(\phi')}\cos(\theta_1 - \beta) + \cos(\theta_0 - \beta)}{\cos(\beta - \sigma)} \tag{A12}$$

$$\frac{L}{r_0} = \frac{3\,e^{(\theta_1 - \theta_0)\tan(\phi')}\left[\sin(\theta_1) - \cos(\theta_1)\tan(\sigma)\right] - \sin(\theta_0) + \cos(\theta_0)\tan(\sigma)}{\sin(\beta)\tan(\sigma) + \cos(\beta)} \tag{A13}$$

The results obtained with equation (A3) indicate that the coefficient K_{Pc} considers Caquot's theorem of corresponding states (Caquot, 1934) through the following relationship:

$$K_{Pc} = \frac{K_{Pq0} - \frac{1}{\cos(\delta)}}{\tan(\phi')} \tag{A14}$$

where

$$K_{Pq0} = -\frac{1}{\frac{l}{r_0}}\frac{f_8}{f_4} \tag{A15}$$

$$f_8 = \frac{L}{r_0}\left[\sin(\beta - \theta_0) + \frac{l}{r_0}\sin(\sigma - \beta) - \frac{1}{2}\frac{L}{r_0}\right] \tag{A16}$$

References

Anagnostopoulos, G. G., Fatichi, S., & Burlando, P. (2015). An advanced process-based distributed model for the investigation of rainfall-induced landslides: The effect of process representation and boundary conditions. *Water Resources Research*, *51*, 7501–7523. https://doi.org/10.1002/2015WR016909

Askarinejad, A., Akca, D., & Springman, S. M. (2018). Precursors of instability in a natural slope due to rainfall: A full-scale experiment. *Landslides*, *15*(9), 1745–1759. https://doi.org/10.1007/s10346-018-0994-0

Askarinejad, A., Casini, F., Bischof, P., Beck, A., & Springman, S. M. (2012). Rainfall induced instabilities: A field experiment on a silty sand slope in northern Switzerland. *Rivista Italiana di Geotecnica*, *3*(12), 50–71.

Bellugi, D., Milledge, D. G., Dietrich, W. E., McKean, J. A., Perron, J. T., Sudderth, E. B., & Kazian, B. (2015). A spectral clustering search algorithm for predicting shallow landslide size and location: A shallow landslide search algorithm. *Journal of Geophysical Research: Earth Surface*, *120*, 300–324. https://doi.org/10.1002/2014JF003137

Bellugi, D., Milledge, D. G., Dietrich, W. E., Perron, J. T., & McKean, J. (2015). Predicting shallow landslide size and location across a natural landscape: Application of a spectral clustering search algorithm. *Journal of Geophysical Research: Earth Surface*, *120*, 2552–2585. https://doi.org/10.1002/2015JF003520

Benmebarek, S., Khelifa, T., Benmebarek, N., & Kastner, R. (2008). Numerical evaluation of 3D passive earth pressure coefficients for retaining wall subjected to translation. *Computers and Geotechnics*, *35*(1), 47–60. https://doi.org/10.1016/j.compgeo.2007.01.008

Benmeddour, D., Mellas, M., Frank, R., & Mabrouki, A. (2012). Numerical study of passive and active earth pressures of sands. *Computers and Geotechnics*, *40*, 34–44. https://doi.org/10.1016/j.compgeo.2011.10.002

Blum, H. (1932). Wirtschaftliche Dalbenformen und dereń Berechnung. *Bautechnik*, *10*(5), 122–135.

Bordoni, M., Meisina, C., Valentino, R., Bittelli, M., & Chersich, S. (2015). Site-specific to local-scale shallow landslides triggering zones assessment using TRIGRS. *Natural Hazards and Earth System Sciences*, *15*(5), 1025–1050. https://doi.org/10.5194/nhess-15-1025-2015

Bowles, J. E. (1997). *Foundation analysis and design* (5th ed., Vol. International Edition). Singapore: The McGraw-Hill Companies, Inc.

Bozorgzadeh, A., Ashford, S. A., & Restrepo, J. I. (2008). Effect of backfill soil type on stiffness and ultimate capacity of bridge abutments. In *Proceedings of the 14th World Conference on Earthquake Engineering* (pp. 1–9). Beijing, China. Retrieved from http://ascelibrary.org/doi/abs/10.1061/40975(318)168

Brenning, A. (2005). Spatial prediction models for landslide hazards: Review, comparison and evaluation. *Natural Hazards and Earth System Sciences*, *5*(6), 853–862. https://doi.org/10.5194/nhess-5-853-2005

Brinch Hansen, J. (1953). *Earth pressure calculation*. Copenhagen, Denmark: The Danish Technical Press.

Burroughs, E. R. (1985). Landslide hazard rating for portions of the Oregon Coast Range. In Proceedings of the Symposium on Effects of Forest Land Use on Erosion and Slope Stability (May 7–11, 1984) (pp. 265–274). Honolulu: University of Hawaii.

Burroughs, E. R., & Thomas, B. R. (1977). *Declining root strength in Douglas-fir after felling as a factor in slope stability* (p. 27). Ogden, Utah U.S.A: Intermountain Forest and Range Experiment Station, Forest Service, U.S. Dept. of Agriculture.

Campbell, R. H. (1975). *Soil slips, debris flows, and rainstorms in the Santa Monica Mountains and vicinity, southern California*, *U.S. Geological Survey Professional Paper, 851* (p. 51). Alexandria, VA: U.S. Government Publishing Office.

Capilleri, P. P., Motta, E., Todaro, M., Massimino, M. R., & Raciti, E. (2015). Studio sperimentale del comportamento di un terreno incoerente in stato passivo soggetto a un carico applicato da una piastra rigida. In *Proceedings of the "Incontro Annuale dei Ricercatori di Ingegneria Geotecnica"*, IARG 2015, Cagliari, Italy (June 24-25, 2015).

Caquot, A. I. (1934). *Équilibre des massifs à frottement interne: stabilité des terres, pulvérulentes ou cohérentes*. Paris, France: Gauthier-Villars.

Caquot, A. I., & Kérisel, J. L. (1948). *Tables for the calculation of passive pressure, active pressure and bearing capacity of foundations*. Paris, France: Gauthier-Villars.

Casadei, M., Dietrich, W. E., & Miller, N. L. (2003). Testing a model for predicting the timing and location of shallow landslide initiation in soil-mantled landscapes. *Earth Surface Processes and Landforms*, *28*(9), 925–950. https://doi.org/10.1002/esp.470

Chen, W. F., & Rosenfarb, J. L. (1973). Limit analysis solution of earth pressure problems. *Soils and Foundations*, *13*(4), 45–60. https://doi.org/10.3208/sandf1972.13.4_45

Cislaghi, A., & Bischetti, G. B. (2019). Source areas, connectivity, and delivery rate of sediments in mountainous-forested hillslopes: A probabilistic approach. *Science of the Total Environment*, *652*, 1168–1186. https://doi.org/10.1016/j.scitotenv.2018.10.318

Cislaghi, A., Chiaradia, E. A., & Bischetti, G. B. (2017). Including root reinforcement variability in a probabilistic 3D stability model. *Earth Surface Processes and Landforms*, *42*(12), 1789–1806. https://doi.org/10.1002/esp.4127

Cislaghi, A., Rigon, E., Lenzi, M. A., & Bischetti, G. B. (2018). A probabilistic multidimensional approach to quantify large wood recruitment from hillslopes in mountainous-forested catchments. *Geomorphology*, *306*, 108–127. https://doi.org/10.1016/j.geomorph.2018.01.009

Cohen, D., & Schwarz, M. (2017). Tree-root control of shallow landslides. *Earth Surface Dynamics*, *5*(3), 451–477. https://doi.org/10.5194/esurf-5-451-2017

Coulomb, C. A. (1776). *Essai sur une application des règles de maximis & minimis à quelques problèmes de statique, relatifs à l'architecture*, *Memoires de l'Academie Royale pres Divers Savants* (Vol. 7, pp. 343–382). Paris, France: De l'Imprimerie Royale.

Craig, R. F. (2013). *Soil mechanics* (p. 419). Boston, MA: Springer.

Cruden, D. M., & Varnes, D. (1996). Landslide types and processes. In A. K. Turner & R. L. Schuster (Eds.), Transportation Research Board National Research Council *Landslides, investigation and mitigation* (Vol. 247, pp. 36–75). Washington, DC: National Academy Press.

Culmann, K. (1886). *Die graphische Statik*. Zurich, Switzerland: Meyer & Zeller.

Das, B. M. (2010). *Principles of geotechnical engineering*. Stamford, CT: Cengage Learning.

Dietrich, W. E., McKean, J., Bellugi, D., & Perron, T. (2007). The prediction of shallow landslide location and size using a multidimensional landslide analysis in a digital terrain model. In *Proceedings of the 4th international conference on debrisflow hazards mitigation: Mechanics, prediction, and assessment (DFHM-4)* (pp. 10–13). Chengdu, China.

Doglioni, A., Galeandro, A., & Simeone, V. (2011). A simple model for passive failure compression structure at the toe of landslide. In *Landslide science and practice* (pp. 177–181). Boston, MA: Springer. Retrieved from http://link.springer.com/chapter/10.1007/978-3-642-31310-3_24

Dorren, L. K. A., & Schwarz, M. (2016). Quantifying the stabilizing effect of forests on shallow landslide-prone slopes. In F. G. Renaud, K. Sudmeier-Rieux, M. Estrella, & U. Nehren (Eds.), *Ecosystem-based disaster risk reduction and adaptation in practice* (Vol. 42, pp. 255–270). Cham: Springer International Publishing. https://doi.org/10.1007/978-3-319-43633-3_11

Duncan, J. M., & Mokwa, R. L. (2001). Passive earth pressures: Theories and tests. *Journal of Geotechnical and Geoenvironmental Engineering*, *127*(3), 248–257. https://doi.org/10.1061/(ASCE)1090-0241(2001)127:3(248)

Fan, L., Lehmann, P., & Or, D. (2016). Effects of soil spatial variability at the hillslope and catchment scales on characteristics of rainfall-induced landslides. *Water Resources Research*, *52*, 1781–1799. https://doi.org/10.1002/2015WR017758

Fang, Y.-S., Chen, J.-M., & Chen, C.-Y. (1997). Earth pressures with sloping backfill. *Journal of Geotechnical and Geoenvironmental Engineering*, *123*(3), 250–259. https://doi.org/10.1061/(ASCE)1090-0241(1997)123:3(250)

Fang, Y.-S., Chen, T.-J., & Wu, B.-F. (1994). Passive earth pressures with various wall movements. *Journal of Geotechnical Engineering*, *120*(8), 1307–1323. https://doi.org/10.1061/(ASCE)0733-9410(1994)120:8(1307)

Fang, Y.-S., Ho, Y.-C., & Chen, T.-J. (2002). Passive earth pressure with critical state concept. *Journal of Geotechnical and Geoenvironmental Engineering*, *128*(8), 651–659. https://doi.org/10.1061/(ASCE)1090-0241(2002)128:8(651)

Frehner, M., Wasser, B., & Schwitter, R. (2005). Sustainability and control method in protection forests. In *Guidelines for silvicultural management in forests with protective function* (Appendix 3, pp. 9–13). Bern, Switzerland: Federal Office for the Environment (FOEN). http://www.schutzwald-schweiz.ch/tl_files/gebirgswald/de/02_NaiS/00_Hauptteil/00_Gesamt/NaiS_D_A_Hauptteil.pdf

Friedli, B., Hauswirth, D., & Puzrinć, A. M. (2017). Lateral earth pressure in constrained landslides. *Géotechnique*, *67*(10), 1–16. https://doi.org/10.1680/jgeot.16.P.158

Ghezzehei, T. A., & Or, D. (2001). Rheological properties of wet soils and clays under steady and oscillatory stresses. *Soil Science Society of America Journal*, *65*(3), 624–637. https://doi.org/10.2136/sssaj2001.653624x

Ghezzehei, T. A., & Or, D. (2003). Stress-induced volume reduction of isolated pores in wet soil. *Water Resources Research*, *39*(3), 1067. https://doi.org/10.1029/2001WR001137

Griffiths, D. V., Huang, J., & de Wolfe, G. F. (2011). Numerical and analytical observations on long and infinite slopes. *International Journal for Numerical and Analytical Methods in Geomechanics*, *35*(5), 569–585. https://doi.org/10.1002/nag.909

Gutberlet, C., Katzenbach, R., & Hutter, K. (2013). Experimental investigation into the influence of stratification on the passive earth pressure. *Acta Geotechnica*, *8*(5), 497–507. https://doi.org/10.1007/s11440-013-0270-3

Guzzetti, F., Carrara, A., Cardinali, M., & Reichenbach, P. (1999). Landslide hazard evaluation: A review of current techniques and their application in a multi-scale study, Central Italy. *Geomorphology*, *31*(1-4), 181–216. https://doi.org/10.1016/S0169-555X(99)00078-1

Hess, D. M., Leshchinsky, B. A., Bunn, M., Benjamin Mason, H., & Olsen, M. J. (2017). A simplified three-dimensional shallow landslide susceptibility framework considering topography and seismicity. *Landslides*, *14*(5), 1677–1697. https://doi.org/10.1007/s10346-017-0810-2

Horn, A. (1972). Résistance et déplacement de culées de ponts chargées latéralement. In *Proceedings of the 5th European Conference on Soil Mechanics and Foundation Engineering* (Vol. 2, pp. 143–145). Madrid, Spain.

Iverson, R. M., Reid, M. E., Iverson, N. R., LaHusen, R. G., Logan, M., Mann, J. E., & Brien, D. L. (2000). Acute sensitivity of landslide rates to initial soil porosity. *Science*, *290*(5491), 513–516. https://doi.org/10.1126/science.290.5491.513

Iverson, R. M. (2000). Landslide triggering by rain infiltration. *Water Resources Research*, *36*(7), 1897–1910. https://doi.org/10.1029/2000WR900090

Janbu, N. (1957). Earth pressure and bearing capacity calculations by generalized procedure of slices. In *Proceedings of the 4th International Conference SMFE* (Vol. 2, pp. 207–212). London.

Kérisel, J., & Absi, E. (1990). *Active and passive earth pressure tables*. Paris, France: CRC Press - Taylor & Francis Group.

Khelifa, T., & Benmebarek, S. (2014). Dilation effect on 3D passive earth pressure coefficients for retaining wall. *Academic Platform Journal of Engineering and Science*, *2*(2), 1–6. https://doi.org/10.5505/apjes.2014.43153

Kim, M. S., Onda, Y., Kim, J. K., & Kim, S. W. (2015). Effect of topography and soil parameterisation representing soil thicknesses on shallow landslide modelling. *Quaternary International*, *384*, 91–106. https://doi.org/10.1016/j.quaint.2015.03.057

Korup, O. (2006). Effects of large deep-seated landslides on hillslope morphology, western Southern Alps, New Zealand. *Journal of Geophysical Research*, *111*. https://doi.org/10.1029/2004JF000242

Korup, O., Densmore, A. L., & Schlunegger, F. (2010). The role of landslides in mountain range evolution. *Geomorphology*, *120*(1–2), 77–90. https://doi.org/10.1016/j.geomorph.2009.09.017

Krey, H., & Ehrenberg, J. (1936). *Erddruck, Erdwiderstand und Tragfähigkeit des Baugrundes* (p. 347). Berlin, Germany: W. Ernst & Sohn.

Kumar, J., & Subba Rao, K. S. (1997). Passive pressure coefficients, critical failure surface and its kinematic admissibility. *Géotechnique*, *47*(1), 185–192. https://doi.org/10.1680/geot.1997.47.1.185

Lange, B., Luescher, P., & Germann, P. (2009). Significance of tree roots for preferential infiltration in stagnic soils. *Hydrology and Earth System Sciences*, *13*(10), 1809–1821. https://doi.org/10.5194/hess-13-1809-2009

Lange, B., Germann, P. F., & Lüscher, P. (2011). Runoff-generating processes in hydromorphic soils on a plot scale: Free gravity-driven versus pressure-controlled flow. *Hydrological Processes*, *25*(6), 873–885. https://doi.org/10.1002/hyp.7873

Larsen, I. J., Montgomery, D. R., & Korup, O. (2010). Landslide erosion controlled by hillslope material. *Nature Geoscience*, *3*(4), 247–251. https://doi.org/10.1038/ngeo776

Lehmann, P., Gambazzi, F., Suski, B., Baron, L., Askarinejad, A., Springman, S. M., et al. (2013). Evolution of soil wetting patterns preceding a hydrologically induced landslide inferred from electrical resistivity survey and point measurements of volumetric water content and pore water pressure. *Water Resources Research*, *49*, 7992–8004. https://doi.org/10.1002/2013WR014560

Lehmann, P., & Or, D. (2012). Hydromechanical triggering of landslides: From progressive local failures to mass release. *Water Resources Research*, *48*, W03535. https://doi.org/10.1029/2011WR010947

Macuh, B., & Škrabl, S. (2010). Passive earth pressure determination: Application of the corresponding state theorem for calculating upper-bound values. *Acta Geotechnica Slovenica*, *2*.

Mao, Z., Saint-André, L., Genet, M., Mine, F.-X., Jourdan, C., Rey, H., et al. (2012). Engineering ecological protection against landslides in diverse mountain forests: Choosing cohesion models. *Ecological Engineering*, *45*, 55–69. https://doi.org/10.1016/j.ecoleng.2011.03.026

Mazindrani, Z. H., & Ganjali, M. H. (1997). Lateral earth pressure problem of cohesive backfill with inclined surface. *Journal of Geotechnical and Geoenvironmental Engineering*, *123*(2), 110–112. https://doi.org/10.1061/(ASCE)1090-0241(1997)123:2(110)

Mergili, M., Marchesini, I., Rossi, M., Guzzetti, F., & Fellin, W. (2014). Spatially distributed three-dimensional slope stability modelling in a raster GIS. *Geomorphology*, *206*, 178–195. https://doi.org/10.1016/j.geomorph.2013.10.008

Milledge, D. G., Bellugi, D., McKean, J. A., Densmore, A. L., & Dietrich, W. E. (2014). A multidimensional stability model for predicting shallow landslide size and shape across landscapes: Predicting landslide size and shape. *Journal of Geophysical Research: Earth Surface*, *119*, 2481–2504. https://doi.org/10.1002/2014JF003135

Milledge, D. G., Griffiths, D. V., Lane, S. N., & Warburton, J. (2012). Limits on the validity of infinite length assumptions for modelling shallow landslides. *Earth Surface Processes and Landforms*, *37*(11), 1158–1166. https://doi.org/10.1002/esp.3235

Montgomery, D. R., & Dietrich, W. E. (1994). A physically based model for the topographic control. *Water Resources Research*, *30*(4), 1153–1171. https://doi.org/10.1029/93WR02979

Montgomery, D. R., Schmidt, K. M., Dietrich, W. E., & McKean, J. (2009). Instrumental record of debris flow initiation during natural rainfall: Implications for modeling slope stability. *Journal of Geophysical Research*, *114*, F01031. https://doi.org/10.1029/2008JF001078

Montgomery, D. R., Schmidt, K. M., Greenberg, H. M., & Dietrich, W. E. (2000). Forest clearing and regional landsliding. *Geology*, *28*(4), 311–314. https://doi.org/10.1130/0091-7613(2000)28<311:FCARL>2.0.CO;2

Morgenstern, N. R., & Eisenstein, Z. (1970). Methods of estimating lateral loads and deformations. In *Proceedings of the ASCE Speciality Conf on Lateral Stresses in the Ground and Design of Earth-Retaining Structures* (pp. 51–102). Ithaca, New York: American Society of Civil Engineers (ASCE).

Motta, E., & Raciti, E. (2014). A closed form solution for a three dimensional passive earth pressure coefficient. *Rivista Italiana Di Geotecnica*, *3*, 18–27.

Müller-Breslau, H. F. B. (1906). *Erddruck auf stuetzmauern*. Stuttgart, Germany: A. Kröner.

Mullins, C. E., & Panayiotopoulos, K. P. (1984). The strength of unsaturated mixtures of sand and kaolin and the concept of effective stress. *Journal of Soil Science*, *35*(3), 459–468. https://doi.org/10.1111/j.1365-2389.1984.tb00303.x

Narain, J., Saran, S., & Nandakumaran, P. (1969). Model study of passive pressure in sand. *Journal of Soil Mechanics & Foundations Division*, *95*(4), 969–984.

Oberender, P. W., & Puzrin, A. M. (2016). Observation-guided constitutive modelling for creeping landslides. *Géotechnique*, *66*(3), 232–247. https://doi.org/10.1680/jgeot.15.LM.003

Ochiai, H., Okada, Y., Furuya, G., Okura, Y., Matsui, T., Sammori, T., et al. (2004). A fluidized landslide on a natural slope by artificial rainfall. *Landslides*, *1*(3), 211–219. https://doi.org/10.1007/s10346-004-0030-4

Pack, R. T., Tarboton, D. G., & Goodwin, C. N. (1998). The SINMAP approach to terrain stability mapping. In Proceedings of the 8th congress of the international association of engineering geology, Vancouver, British Columbia, Canada (pp. 21–25). Retrieved from http://www.crwr.utexas.edu/gis/gishydro99/uwrl/sinmap/iaeg.pdf

Patki, M. A., Mandal, J. N., & Dewaikar, D. M. (2015). Computation of passive earth pressure coefficients for a vertical retaining wall with inclined cohesionless backfill. *International Journal of Geo-Engineering*, *6*(1). https://doi.org/10.1186/s40703-015-0004-5

Penna, D., Borga, M., Aronica, G. T., Brigandì, G., & Tarolli, P. (2014). The influence of grid resolution on the prediction of natural and road-related shallow landslides. *Hydrology and Earth System Sciences*, *18*(6), 2127–2139. https://doi.org/10.5194/hess-18-2127-2014

Poterasu, A. (2013). Experimental investigation of the passive Earth pressure on retaining wall when the backfill is collapsible soil (Master thesis). Concordia University. Retrieved from http://spectrum.library.concordia.ca/977883/

Potyondy, J. G. (1961). Skin friction between various soils and construction materials. *Géotechnique*, *11*(4), 339–353. https://doi.org/10.1680/geot.1961.11.4.339

Pradhan, B. (2010). Remote sensing and GIS-based landslide hazard analysis and cross-validation using multivariate logistic regression model on three test areas in Malaysia. *Advances in Space Research*, *45*(10), 1244–1256. https://doi.org/10.1016/j.asr.2010.01.006

Prancevic, J. P., Lamb, M. P., Palucis, M. C., & Venditti, J. G. (2018). The role of three-dimensional boundary stresses in limiting the occurrence and size of experimental landslides. *Journal of Geophysical Research: Earth Surface*, *123*, 46–65. https://doi.org/10.1002/2017JF004410

Puzrin, A. M., & Sterba, I. (2006). Inverse long-term stability analysis of a constrained landslide. *Géotechnique*, *56*(7), 483–489. https://doi.org/10.1680/geot.2006.56.7.483

Puzrin, A. M., & Schmid, A. (2011). Progressive failure of a constrained creeping landslide. *Proceedings of the Royal Society A: Mathematical, Physical and Engineering Sciences*, *467*(2133), 2444–2461. https://doi.org/10.1098/rspa.2011.0063

Puzrin, A. M., & Schmid, A. (2012). Evolution of stabilised creeping landslides. *Géotechnique*, *62*(6), 491–501. https://doi.org/10.1680/geot.11.P.041

Rankine, W. J. M. (1857). On the stability of loose earth. *Philosophical Transactions of the Royal Society of London*, *147*, 9–27.

Rebhann, G. (1871). *Theorie des Erddruckes und der Futtermauern*. Wien: C. Gerold's sohn.

Regenass, P., Meksaouine, M., Kastner, R., Soubra, A.-H., & Bourdeau, Y. (2000). Étude de la butée sur un écran de largeur limitée en sol frottant. *Revue française de génie civil*, *4*(4), 543–576. https://doi.org/10.1080/12795119.2000.9692286

Reneau, S. L., & Dietrich, W. E. (1987). Size and location of colluvial landslides in a steep forested landscape. *IAHS-AISH Publication*, *165*, 39–48.

Riestenberg, M. M., & Sovonick-Dunford, S. (1983). The role of woody vegetation in stabilizing slopes in the Cincinnati area, Ohio. *Geological Society of America Bulletin*, *94*(4), 506–518. https://doi.org/10.1130/0016-7606(1983)94<506:TROWVI>2.0.CO;2

Roering, J. J., Kirchner, J. W., & Dietrich, W. E. (2001). Hillslope evolution by nonlinear, slope-dependent transport: Steady state morphology and equilibrium adjustment timescales. *Journal of Geophysical Research*, *B8*, 16,499–16,513.

Roering, J. J., Kirchner, J. W., & Dietrich, W. E. (2005). Characterizing structural and lithologic controls on deep-seated landsliding: Implications for topographic relief and landscape evolution in the Oregon Coast Range, USA. *Geological Society of America Bulletin*, *117*(5), 654–668. https://doi.org/10.1130/B25567.1

Rollins, K. M., & Cole, R. T. (2006). Cyclic lateral load behavior of a pile cap and backfill. *Journal of Geotechnical and Geoenvironmental Engineering*, *132*(9), 1143–1153. https://doi.org/10.1061/(ASCE)1090-0241(2006)132:9(1143)

Rowe, P. W., & Peaker, K. (1965). Passive earth pressure measurements. *Géotechnique*, *15*(1), 57–78. https://doi.org/10.1680/geot.1965.15.1.57

Savage, W., & Wasowski, J. (2006). A plastic flow model for the Acquara–Vadoncello landslide in Senerchia, Southern Italy. *Engineering Geology*, *83*(1–3), 4–21. https://doi.org/10.1016/j.enggeo.2005.06.024

Savage, W. Z., & Smith, W. K. (1986). *A model for the plastic flow of landslides (U.S. Geological survey professional paper No. 1385)*, (p. 38). Washington, DC: U.S. Geological Survey Federal Center.JF.

Schmidt, K. M., Roering, J. J., Stock, J. D., Dietrich, W. E., Montgomery, D. R., & Schaub, T. (2001). The variability of root cohesion as an influence on shallow landslide susceptibility in the Oregon Coast Range. *Canadian Geotechnical Journal*, *38*(5), 995–1024. https://doi.org/10.1139/cgj-38-5-995

Schwarz, M., Cohen, D., & Or, D. (2011). Pullout tests of root analogs and natural root bundles in soil: Experiments and modeling. *Journal of Geophysical Research*, *116*, F02007. https://doi.org/10.1029/2010JF001753

Schwarz, M., Giadrossich, F., & Cohen, D. (2013). Modeling root reinforcement using a root-failure Weibull survival function. *Hydrology and Earth System Sciences*, *17*(11), 4367–4377. https://doi.org/10.5194/hess-17-4367-2013

Schwarz, M., Rist, A., Cohen, D., Giadrossich, F., Egorov, P., Büttner, D., et al. (2015). Root reinforcement of soils under compression. *Journal of Geophysical Research: Earth Surface*, *120*, 2103–2120. https://doi.org/10.1002/2015JF003632

Sdao, F., & Simeone, V. (2007). Mass movements affecting Goddess Mefitis sanctuary in Rossano di Vaglio (Basilicata, southern Italy). *Journal of Cultural Heritage*, *8*(1), 77–80. https://doi.org/10.1016/j.culher.2006.10.004

Sherif, M. A., Ishibashi, I., & Lee, C. D. (1982). Earth pressure against rigid retaining walls. *Journal of Geotechnical and Geoenvironmental Engineering*, *108*.

Shiau, J. S., Augarde, C. E., Lyamin, A. V., & Sloan, S. W. (2008). Finite element limit analysis of passive earth resistance in cohesionless soils. *Soils and Foundations*, *48*(6), 843–850. https://doi.org/10.3208/sandf.48.843

Shroder, J. F. J., & Bishop, M. P. (1998). Mass movement in the Himalaya: New insights and research directions. *Geomorphology*, *26*(1–3), 13–35. https://doi.org/10.1016/S0169-555X(98)00049-X

Sidle, R. C., & Ochiai, H. (2006). *Landslides: processes, prediction, and land use* (Vol. 18). Washington, DC: American Geophysical Union. https://doi.org/10.1029/WM018

Sidle, R. C., Pearce, A. J., & O'Loughlin, C. L. (1985). *Hillslope stability and land use*. Washington, DC: American Geophysical Union. https://doi.org/10.1029/WM011

Škrabl, S. (2008). The limit values and the distribution of three-dimensional passive earth pressures. *Acta Geotechnica Slovenica*, *1*, 23–34.

Škrabl, S., & Macuh, B. (2005). Upper-bound solutions of three-dimensional passive earth pressures. *Canadian Geotechnical Journal*, *42*(5), 1449–1460. https://doi.org/10.1139/t05-067

Soubra, A.-H., Kastner, R., & Benmansour, A. (1999). Passive earth pressures in the presence of hydraulic gradients. *Géotechnique*, *49*(3), 319–330. https://doi.org/10.1680/geot.1999.49.3.319

Soubra, A.-H., & Macuh, B. (2002). Active and passive earth pressure coefficients by a kinematical approach. *Proceedings of the ICE-Geotechnical Engineering*, *155*(2), 119–131. https://doi.org/10.1680/geng.155.2.119.38657

Soubra, Abdul-Hamid, Galvani, D., & Regenass, P. (2000). Three-dimensional active earth pressures. In *European Congress on Computational Methods in Applied Sciences and Engineering ECCOMAS* 2000. Barcelona. Retrieved from http://congress.cimne.com/eccomas/eccomas2000/pdf/561.pdf

Soubra, A.-H., & Regenass, P. (2000). Three-dimensional passive earth pressures by kinematical approach. *Journal of Geotechnical and Geoenvironmental Engineering*, *126*(11), 969–978. https://doi.org/10.1061/(ASCE)1090-0241(2000)126:11(969)

Tarolli, P., & Tarboton, D. G. (2006). A new method for determination of most likely landslide initiation points and the evaluation of digital terrain model scale in terrain stability mapping. *Hydrology and Earth System Sciences Discussions*, *10*(5), 663–677. https://doi.org/10.5194/hess-10-663-2006

Taylor, D. W. (1948). Fundamentals of soil mechanics. *Soil Science*, *66*(2), 161. https://doi.org/10.1097/00010694-194808000-00008

Terwilliger, V. J., & Waldron, L. J. (1991). Effects of root reinforcement on soil-slip patterns in the Transverse Ranges of southern California. *Geological Society of America Bulletin*, *103*(6), 775–785. https://doi.org/10.1130/0016-7606(1991)103<0775:EORROS>2.3.CO;2

Terzaghi, K. (1920). Old earth pressure theories and new test results. *Engineering News-Record*, *85*(14), 632–637.

Terzaghi, K. (1941). General wedge theory of earth pressure. *Transactions of the American Society of Civil Engineers*, *106*(1), 68–80.

Terzaghi, K. (1943). *Theoretical soil mechanics*. New York: John Wiley & Sons. https://doi.org/10.1002/9780470172766

Terzaghi, K., Peck, R. B., & Mesri, G. (1996). *Soil mechanics in engineering practice*. New York: John Wiley & Sons.

van Beek, L. P. H., & van Asch, T. W. J. (2004). Regional assessment of the effects of land-use change on landslide hazard by means of physically based modelling. *Natural Hazards*, *31*(1), 289–304. https://doi.org/10.1023/B:NHAZ.0000020267.39691.39

von Ruette, J., Lehmann, P., & Or, D. (2013). Rainfall-triggered shallow landslides at catchment scale: Threshold mechanics-based modeling for abruptness and localization. *Water Resources Research*, *49*, 6266–6285. https://doi.org/10.1002/wrcr.20418

Vrecl-Kojc, H., & Škrabl, S. (2007). Determination of passive earth pressure using three-dimensional failure mechanism. *Acta Geotechnica Slovenica*, *4*(1), 11–23.

Wilson, P., & Elgamal, A. (2010). Passive earth pressure force-displacement relationships. In *Proceedings of the 5th International Conference on Recent Advances in Geotechnical Earthquake Engineering and Soil* Dynamics (pp. 1–11). San Diego, CA.

Wilson, P. R. (2009). Large scale passive force-displacement and dynamic earth pressure experiments and simulations (PhD dissertation). University of California, San Diego, CA. Retrieved from http://escholarship.org/uc/item/16g547dp

Wu, T. H., McOmber, R. M., Erb, R. T., & Beal, P. E. (1988). Study of soil-root interaction. *Journal of Geotechnical Engineering*, *114*(12), 1351–1375. https://doi.org/10.1061/(ASCE)0733-9410(1988)114:12(1351)

Wu, W., & Sidle, R. C. (1995). A distributed slope stability model for steep forested basins. *Water Resources Research*, *31*(8), 2097–2110. https://doi.org/10.1029/95WR01136